Production of protons, deuterons and tritons in argon-nucleus interactions at 3.2A GeV

BM@N Collaboration

Abstract

Results of the BM@N experiment at the Nuclotron/NICA complex are presented on proton , deuteron and triton production in interactions of an argon beam of 3.2A GeV with fixed targets of C, Al, Cu, Sn and Pb. Transverse mass spectra, rapidity distributions and multiplicities of protons, deuterons and tritons are measured. The results are treated within a coalescence approach and compared with predictions of theoretical models and with other measurements.

1 Introduction

BM@N (Baryonic Matter at Nuclotron) is the first operational experiment at the Nuclotron/NICA accelerator complex. The Nuclotron provides beams of a variety of particles, from proton up to gold ions, with kinetic energy in the range from 1 to 6 GeV/nucleon for light ions with Z/A ratio of ~ 0.5 and up to 4.5 GeV/nucleon for heavy ions with Z/A ratio of ~ 0.4. At these energies, the nucleon density in the fireball created in the collisions of a heavy-ion beam with fixed targets is 3-4 times higher than the nuclear saturation density [1], thus allowing studying heavy-ion interactions in the regime of high-density baryonic matter [2–5].

In the commissioning phase, in a configuration with limited phase-space coverage, BM@N collected first data with beams of carbon, argon, and krypton ions [6, 7]. In the first physics paper BM@N reported on studies of π^+ and K^+ production in argon-nucleus interactions [8]. This paper presents results on proton, deuteron and triton production in 3.2A GeV argon-nucleus interactions.

At the Nuclotron energies, baryon transfer over finite rapidity distances (baryon stopping [9]) plays an important role [10]- [12]. The baryon density, attained in high energy nuclear collisions, is a crucial quantity governing the reaction dynamics and the overall system evolution, including eventual phase transitions. The baryon rapidity distributions in heavy ion collisions for different combinations of projectile and target as well as at different impact parameters provide essential constrains on the dynamical scenarios of baryon stopping. The BM@N experimental arrangement makes it possible to measure the distribution of protons and light nuclei (d, t) over the rapidity interval [1.0 - 2.2]. This rapidity range is wide enough to include not only the midrapidity (y_{CM} = 1.08), but also the beam rapidity region (y_{beam} = 2.16), in contrast to the collider experiments, where the acceptance is usually focused only in the mid-rapidity region. Together with a sufficient p_T-coverage for nuclear clusters, it is possible at BM@N to better determine the shape of the rapidity density distribution and derive information about rapidity and energy loss in the reaction.

Nuclear cluster production allows one to estimate the nucleon phase-space density attained in the reaction [13]. It governs the overall evolution of the reaction process and may provide information about freeze-out conditions and entropy production in relativistic nucleus-nucleus interactions. A way to measure the nucleon phase-space density is a study of the ratio of deuteron and proton abundances. One of the goals of this work is a study of particle phase-space density evolution in Ar+A collisions for different projectile-target combinations and as a function of collision centrality.

In the framework of statistical thermal models, hadron and light nuclei abundances are predicted to be dependent on the bulk parameters of the fireball: the freeze-out temperature T and baryochemical potential μ [14]. The ratio μ/T can be extracted from the characteristic parameter (penalty factor) describing the mass dependence of the cluster yield [15]. In this paper, we study the system size and mass dependence of cluster production to get insight into the thermal parameters of the particle source.

In collisions of heavy nuclei at relativistic energies, a significant fraction of the initial kinetic energy transforms into particle production and thermal excitation of matter. Various dynamical models, including those based on hydrodynamics, have demonstrated that the entropy per baryon, S/A, created during the initial interaction stage remains constant during the subsequent evolution of the system [16,17]. Thus, data about entropy production can provide information not only about the nucleon phase-space density at the final moments of the reaction (freezeout), but also about the medium properties during the hot and compressed stage. It is also the aim of this work to study the evolution of the entropy in the reaction zone with system size in argon-nucleus collisions and compare BM@N results with other existing experimental data.

The binding energies of deuterons and tritons are small compared to freeze-out temperatures, which are on the order of 100 MeV. These light clusters are therefore not expected to survive through the high density stages of the collision. The deuterons and tritons observed in the experiment are formed and emitted at the end of freeze-out process, and they mainly carry information about this late stage of the collision.

Light cluster production at low energy heavy ion collisions is well described in a simple coalescence model [18–20] through the distributions of their constituents (protons and neutrons) and a coalescence parameter B_A related to the size A of the cluster. To describe heavy-ion collisions at high energies the simple coalescence model is modified taking into account the nucleon phase space distributions at freeze-out as well as the strength of momentum-space correlations induced by collective flow [21]. In central heavy-ion collisions the pressure gradient in the system generates strong transverse radial flow. Therefore nucleon clusters inside a collective velocity field acquire additional momentum proportional to the cluster's mass.

The paper is organized as follows. Section 2 describes the experimental set-up and Section 3 is devoted to details of the event reconstruction. Section 4 describes the evaluation of the proton, deuteron and triton reconstruction efficiency. Section 5 explains the methodology for the definition of centrality classes. Section 6 addresses the evaluation of the cross sections, multiplicities and systematic uncertainties. Transverse mass distributions and rapidity spectra of protons, deuterons and tritons are given in Section 7. The BM@N results are compared with predictions of the DCM-SMM [22, 23] and PHQMD [24] models. Ratios of the transverse momentum distributions of deuterons and tritons to protons are treated within a coalescence approach in Section 8. The results are compared with other experimental data on nucleus-nucleus interactions. Results on baryon rapidity loss in argon-nucleus interactions are presented in Section 9. The compound ratios of yields of protons and tritons to deuterons are presented in section 10. Finally, a summary is given in Section 11.

2 Experimental set-up

The BM@N detector is a forward spectrometer covering the pseudorapidity range $1.6 \leq \eta \leq 4.4$. A schematic view of the BM@N setup in the argon-beam run is shown in Fig. 1. More details of all components of the set-up can be found in [25, 26]. The spectrometer includes a central tracking system consisting of 3 planes of forward silicon-strip detectors (ST) and 6 planes of detectors based on gas electron multipliers (GEM) [27]. The central tracking system is located downstream of the target region inside of a dipole magnet with a bending power of about $\approxeq 2.1$Tm and with a gap of 1.05 m between the poles . In the measurements reported here, the central tracker covered only the upper half of the magnet acceptance.

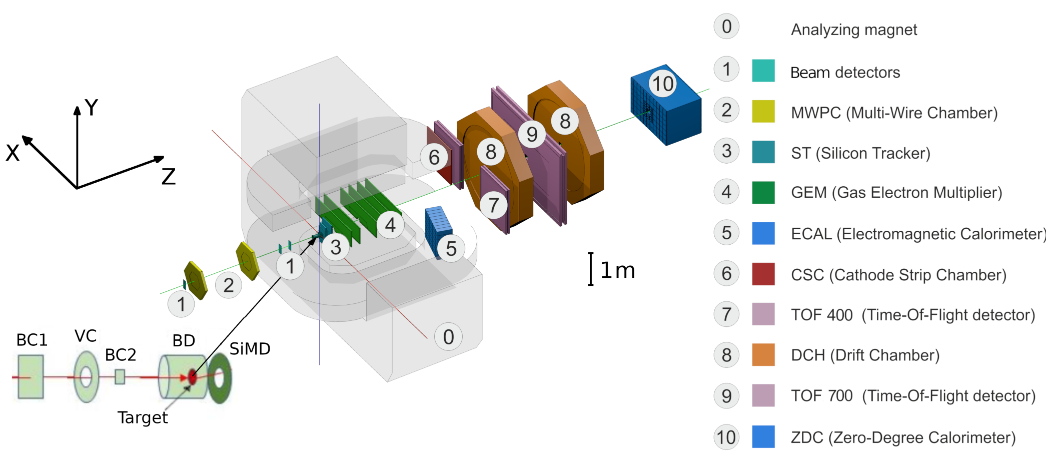

Figure 1: Schematic view of the BM@N setup in the argon beam run.

Two sets of drift chambers (DCH), a cathode strip chamber (CSC), two sets of time-of-flight detectors (ToF), and a zero-degree calorimeter (ZDC) are located downstream of the dipole magnet. The tracking system measures the momentum of charged particles with a relative uncertainty that varies from 2.5% at a momentum of 0.5 GeV/c to 2% from 1 to 2 GeV/c and rises linearly to 6.5% at 5 GeV/c. The time resolutions of the ToF-400 [28] and ToF-700 [29] systems are 84 ps and 115 ps, respectively [30].

Two beam counters (BC1, BC2), a veto counter (VC), a barrel detector (BD), and a silicon multiplicity detector (SiMD) are used for event triggering and for measurement of the incoming beam ions. The BC2 counter provides also the start time T0 for the time-of-flight measurement. The BD detector consists of 40 azimuthal scintillating strips arranged around the target, and the SiMD detector consists of 60 azimuthal silicon segments situated behind the target.

Data were collected with an argon beam intensity of a few 10^5 ions per spill and a spill duration of 2–2.5 sec. The kinetic energy of the beam was 3.2A GeV with a spread of about 1%. A set of solid targets of various materials (C, Al, Cu, Sn, Pb) with an interaction length of 3% was used. The experimental data correspond to a total integrated luminosity of 7.8 $\mu\mathrm{b}^{-1}$ collected with the different targets: 2.1 $\mu\mathrm{b}^{-1}$ (C), 2.3 $\mu\mathrm{b}^{-1}$ (Al), 1.8 $\mu\mathrm{b}^{-1}$ (Cu), 1.1 $\mu\mathrm{b}^{-1}$ (Sn), 0.5 $\mu\mathrm{b}^{-1}$ (Pb). A total of 16.3M argon-nucleus collisions at 3.2A GeV were reconstructed.

To count the number of beam ions that passed through the target, a logical beam trigger BT = BC1$\wedge\overline{\mathrm{VC}}\wedge$BC2 was used. The following logic conditions were applied to generate the trigger signal: 1) BT$\wedge$(BD$\geq 3, 4$); 2) BT$\wedge$(SiMD$\geq 3, 4$); 3) BT$\wedge$(BD$\geq$ 2)$\wedge$(SiMD$\geq$ 3). The trigger conditions were varied to find the optimal ratio between the event rate and the trigger efficiency for each target. Trigger condition 1 was applied for 60% of the data collected with the carbon target. This trigger fraction was continuously reduced with the atomic weight of the target down to 26% for the Pb target. The fraction of data collected with trigger condition 2 was increased from 6% for the carbon target up to 34% for the Pb target. The rest of the data were collected with trigger condition 3.

3 Event reconstruction

Track reconstruction in the central tracker is based on a “cellular automaton” approach [31] implementing a constrained combinatorial search of track candidates with their subsequent fitting by a Kalman filter to determine the track parameters. These tracks are used to reconstruct primary and secondary vertices as well as global tracks by extrapolation and matching to hits in the downstream detectors (CSC, DCH and ToF).

The primary collision vertex position (PV) is measured with a resolution of 2.4 mm in the X-Y plane perpendicular to the beam direction and 3 mm in the beam direction.

Charged particles (protons, deuterons, tritons) are identified using the time of flight Δt measured between T0 and the ToF detectors, the length of the trajectory Δl and the momentum p reconstructed in the central tracker. Then the squared mass M^2 of the particle is calculated by the formula: $M^2 = p^2((\Delta tc/\Delta l)^2 - 1)$, where c is the speed of light.

The following criteria are required for selecting proton, deuteron and triton candidates:

- Each track has at least 4 hits in the GEM detectors (6 detectors in total) [27]. Hits in the forward silicon detectors are used to reconstruct the track, but no requirements are applied to the number of hits;

- Tracks originate from the primary vertex. The deviation of the reconstructed vertex from the nominal target position $Z_{\rm ver}$ along the beam direction is limited to -3.4 cm $< Z_{\rm ver} - Z_0 <$ 1.7 cm. The upper limit corresponds to $\sim 5.7\sigma$ of the Z_{ver} spread and cuts off interactions with the trigger detector located 3 cm behind the target. The beam interaction rate with the trigger detector is well below 1% and was not simulated since it does not affect the precision in Monte Carlo simulation.

- Distance from the track to the primary vertex in the X-Y plane at $Z_{\rm ver}$(DCA) is required to be less than 1 cm, which corresponds to 4σ of the vertex resolution in the X-Y plane;

- Momentum range of positively charged particles is limited by the acceptance of the ToF-400 and ToF-700 detectors to $p > 0.5$ GeV/c and $p > 0.7$ GeV/c, respectively;

- Distance of extrapolated tracks to the CSC (DCH) hits as well as to the ToF-400 (ToF-700) hits should be within $\pm 2.5\sigma$ of the momentum dependent hit-track residual distributions.

The mass squared (M^2) spectra of positively charged particles produced in interactions of the 3.2A GeV argon beam with various targets are shown in Figs. 2a and 2b for ToF-400 and ToF-700 data, respectively. Particles that satisfy the above selection criteria contribute to the M^2 spectra. The proton, deuteron and triton signals are extracted in the M^2 windows which depend on rapidity and at the maximal rapidity extend from 0.4-1.7 (GeV/c^2)^2, 2.3-5.0 (GeV/c^2)^2 and 6.6-10.0 (GeV/c^2)^2, respectively. The signals of protons, deuterons and tritons and their statistical errors are calculated according to the formulae: $sig = hist - bg$, $err_{stat} = \sqrt{hist + \delta bg}$, where $hist$ denotes the histogram integral yield within the selected M^2-window and δbg is the background normalization uncertainty.

(a) (b)

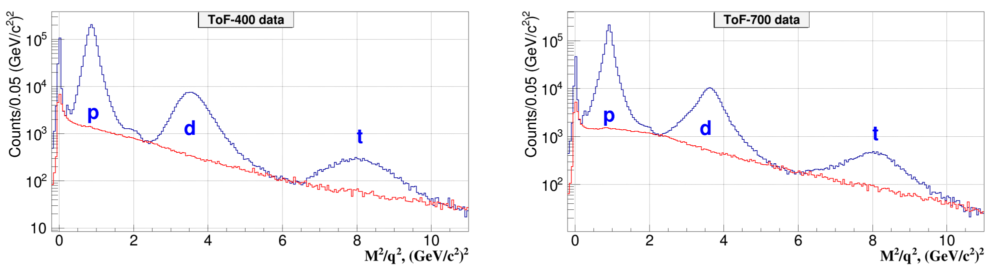

Figure 2: M^2 spectra of positively charged particles produced in argon-nucleus interactions and measured in the ToF-400 (a) and ToF-700 (b) detectors. Peaks of protons, deuterons, and tritons are indicated. The red histograms show the background estimated from "mixed events".

The shape of the background under the proton, deuteron and triton signals in the M^2 spectra is estimated using the "mixed event" method. For that, tracks reconstructed in the central tracker are matched to hits in the ToF detectors taken from different events containing a similar number of tracks. The "mixed event" background is normalized to the integral of the signal histogram outside the M^2 windows of protons, deuterons and tritons. It is found that the background level differs for light and heavy targets and for different intervals of rapidity and transverse momentum.

The ToF-400 and ToF-700 detectors cover different ranges of rapidity and transverse momentum of detected particles. Fig. 3 shows the deuterons measured in ToF-400 and ToF-700 in the rapidity vs transverse momentum plane in Ar+Sn interactions before making efficiency corrections.

The dE/dx information from the GEM detectors is used to separate the deuteron signals from the He^4 signals. The fraction of He^4 in the total $He^4 + d$ sample is determined in rapidity and transverse momentum bins and subtracted from the data signals. The He^4 fraction combined for all the targets is presented in Fig. 4. In most of the $y - p_T$ bins the He^4 fraction does not exceed 3%, only in a few

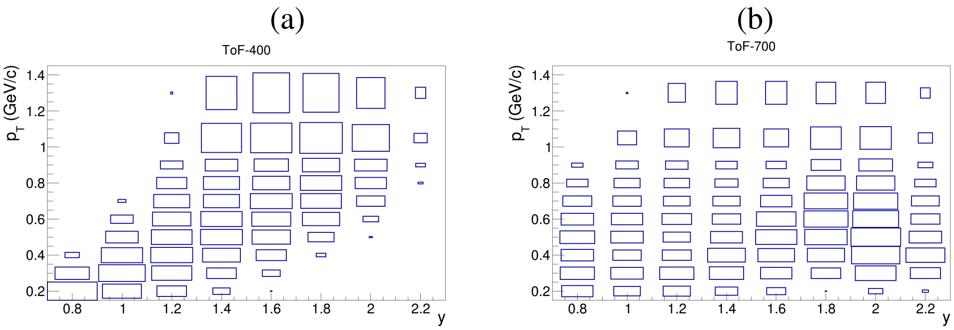

Figure 3: Distribution of the deuteron signals measured in ToF-400 (a) and ToF-700 (b) in the rapidity vs transverse momentum plane in Ar+Sn interactions.

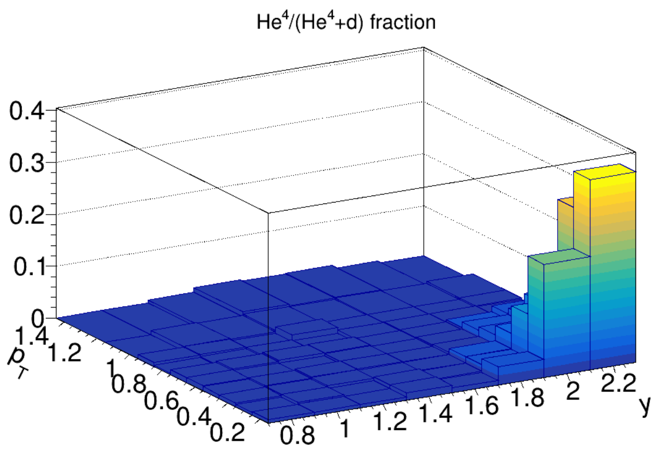

Figure 4: Fraction of He^4 in the $He^4 + d$ sample measured in the rapidity vs transverse momentum plane in Ar+A interacions.

bins at large y and low p_T it reaches 20-35%.

4 Reconstruction efficiency and trigger performance

To evaluate the proton, deuteron and triton reconstruction efficiency, Monte Carlo data samples of argon-nucleus collisions were produced with the DCM-SMM event generator. Propagation of particles through the entire detector volume and responses of the detectors were simulated using the GEANT3 program [32] integrated into the BmnRoot software framework [33].

The Monte Carlo events went through the same chain of reconstruction and identification as the experimental events. The efficiencies of the silicon, GEM, CSC, DCH and ToF detectors were adjusted in the simulation in accordance with the measured detector efficiencies [34]. More details of the simulation are given in ref. [8].

The proton, deuteron and triton reconstruction efficiencies are calculated in intervals of rapidity y and transverse momentum p_T. The reconstruction efficiency includes geometrical acceptance, detector efficiency, kinematic and spatial cuts, and the loss of protons, deuterons and tritons due to in-flight interactions. Figure 5 shows the reconstruction efficiencies of protons (left panels) and deuterons (right panels) in ToF-400 and ToF-700 as functions of y (upper panels) and p_T (lower panels) for Ar+Sn interactions.

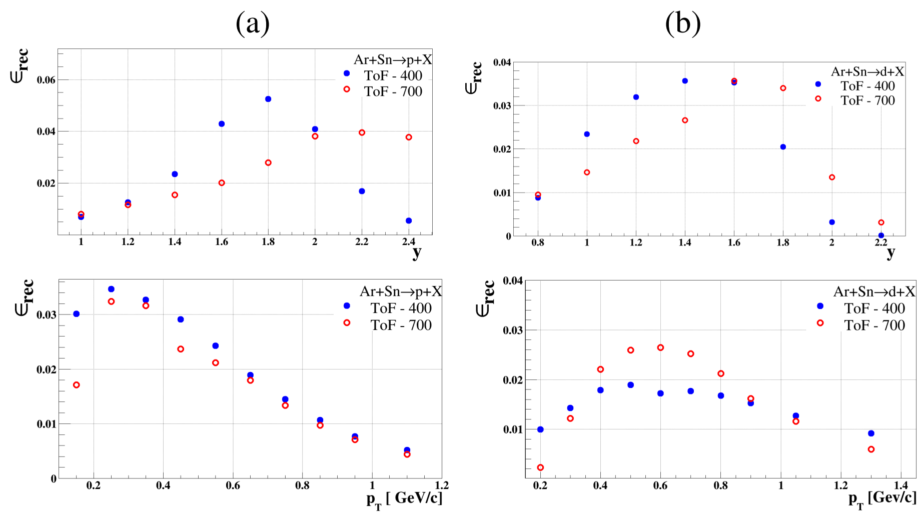

Figure 5: Reconstruction efficiency of protons (a) and deuterons (b) produced in Ar+Sn collisions, detected in ToF-400 (full blue circles) and ToF-700 (open red circles) as functions of rapidity y and p_T. The efficiency includes both acceptance and reconstruction.

The trigger efficiency ϵ_{trig} depends on the number of fired channels in the BD (SiMD) detectors. It was calculated for events with reconstructed protons, deuterons and tritons using event samples recorded with an independent trigger based on the SiMD (BD) detectors. The BD and SiMD detectors cover different and non-overlapping regions of the BM@N acceptance, that is, they detect different collision products.

The efficiency of the combined BD and SiMD triggers was calculated as the product of the efficiencies of the BD and SiMD triggers. The trigger efficiency decreases with a decrease in the mass of the target and an increase in the centrality of the collision. More details of the trigger efficiencies evaluation are given in ref. [8]. In particular, the trigger system accepts events in the whole centrality range, as it is illustrated in Fig. 10 of [8].

5 Centrality classes

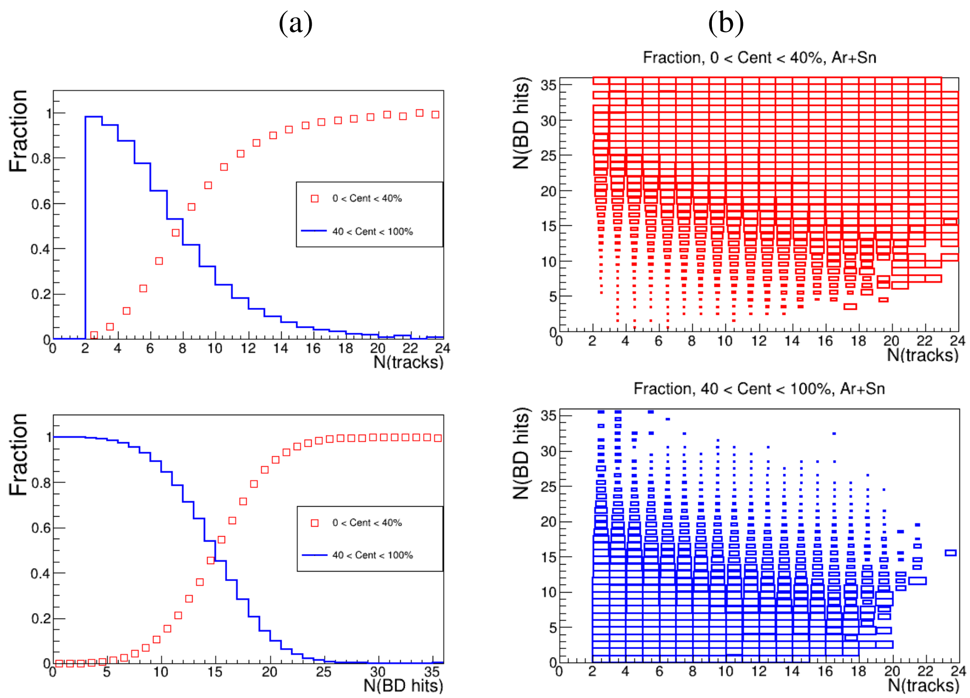

Figure 6: (a) Probability distribution of the number of tracks N(tracks) in the primary vertex (upper panel) and the number of hits N(BD) in the BD detector (lower panel) for events with centrality 0-40% (red open symbols) and 40-100% (blue histogram). (b) two-dimensional plot of the probability distribution of N(tracks) (horizontal axis) vs. N(BD) (vertical axis) in events with centrality 0-40% (upper panel) and 40-100% (lower panel).

The event centrality is determined as the fraction of the interaction cross section in the interval $[0, \mathrm{b}]$ of the impact parameter b of the nucleus-nucleus collision to the total inelastic interaction cross section. Two classes of centrality: 1) 0-40% of the cross section (more central collisions) and 2) 40-100% of the cross section (more peripheral collisions), are defined from the impact parameter distributions of Ar+A inelastic interactions simulated by the DCM-SMM model. The boundary impact parameter b_{cut} for the definition of the two classes for interactions of Ar with various targets is given in Table 1. It was found that the number of tracks originating from the primary event vertex N(tracks) and the number of hits in the Barrel Detector N(BD) are anti-correlated with the impact parameter b. Using results of the DCM-SMM Monte Carlo simulation, the fractions of reconstructed events, which belong to the centrality classes 0-40% and 40-100%, are calculated. Fractions of events with centrality 0-40% and 40-100% are presented in Fig. 6 as functions of N(tracks) , N(BD) and as a two-dimensional distribution N(tracks) / N(BD).

Table 1: The boundary impact parameter b_{cut} for the definition of the two centrality classes 0-40% and 40-100%, and the inclusive inelastic cross section σ_{inel} for Ar+A interactions.

	Ar+C	Ar+Al	Ar+Cu	Ar+Sn	Ar+Pb
b_{cut}, fm	4.23	4.86	5.66	6.32	7.10
σ_{inel}, mb [35]	1470 ± 50	1860 ± 50	2480 ± 50	3140 ± 50	3940 ± 50

Fractions (probabilities) of events with centrality 0-40% and 40-100%, taken from the two-dimensional N(tracks) / N(BD) distributions are used as event weights to define the weighted number of reconstructed protons, deuterons and tritons in the y and p_T bins in data and simulation. The systematic uncertainty of the event centrality is estimated from the remaining difference in the shape of the N(tracks) and N(BD) distributions in y and p_T bins in the simulation relative to the data.

6 Cross sections, multiplicities, and systematic uncertainties

The protons, deuterons and tritons in Ar+C, Al, Cu, Sn, Pb interactions are measured in the following kinematic ranges: transverse momentum $0.1 < p_T < 1.2$ GeV/c (protons), $0.15 < p_T < 1.45$ GeV/c (deuterons), $0.2 < p_T < 1.6$ GeV/c (tritons) and rapidity in the laboratory frame $0.9 < y < 2.5$ (protons), $0.7 < y < 2.3$ (deuterons), $0.7 < y < 2.1$ (tritons). The differential cross sections

$d^2\sigma_{p,d,t}(y,p_T)/dydp_T$ and multiplicities $d^2N_{p,d,t}(y,p_T)/dydp_T$ of protons, deuterons and tritons produced in Ar+C, Al, Cu, Sn, Pb interactions are calculated using the relations:

$$d^2\sigma_{p,d,t}(y,p_T)/dydp_T = \Sigma[d^2n_{p,d,t}(y,p_T,N_{tr})/(\epsilon_{trig}(N_{tr})dydp_T)] \times 1/(L\epsilon^{rec}_{p,d,t}(y,p_T))$$

$$d^2N_{p,d,t}(y,p_T)/dydp_T = d^2\sigma_{p,d,t}(y,p_T)/(\sigma_{inel}dydp_T) \quad (1)$$

where the sum is performed over bins of the number of tracks in the primary vertex, N_{tr}, $n_{p,d,t}(y,p_T,N_{tr})$ is the number of reconstructed protons, deuterons and tritons in the intervals dy and dp_T, $\epsilon_{trig}(N_{tr})$ is the track-dependent trigger efficiency, $\epsilon^{rec}_{p,d,t}(y,p_T)$ is the reconstruction efficiency of protons, deuterons and tritons, L is the luminosity and σ_{inel} is the inelastic cross section for argon-nucleus interactions. The cross sections and multiplicities are evaluated for the two centrality classes: 0-40% and 40-100%.

Table 2: Mean systematic uncertainties averaged over the y, p_T ranges of protons, deuterons and tritons measured in argon-nucleus interactions.

	Ar+C %	Ar+Al %	Ar+Cu %	Ar+Sn %	Ar+Pb %
ϵ_{trig} p,d,t	9	7	7	7	7
protons					
n_p, ϵ_{rec}	15	6	8	14	11
Total	18	9	11	16	13
deuterons					
n_d, ϵ_{rec}	32	22	20	19	22
Total	33	23	21	20	23
tritons					
n_t, ϵ_{rec}	43	22	20	20	22
Total	44	23	21	21	23

Several sources are considered for the evaluation of the systematic uncertainty of the proton, deuteron and triton yield, $n_{p,d,t}$, and the reconstruction efficiency ϵ_{rec}. Some of them affect both the yield $n_{p,d,t}$ and the reconstruction efficiency, ϵ_{rec}. For these cases the correlated effect is taken into account by considering the variations on the $n_{p,d,t}/\epsilon_{rec}$ ratio. A detailed discussion of the systematic uncertainties associated with track reconstruction as well as with the trigger efficiency are given in ref. [8]. Additional sources specific to this analysis are listen below:

- Systematic uncertainty of the background subtraction in the mass-squared M^2 spectra of identified particles: it is estimated as the difference between the background integral under the p, d, t mass-squared windows taken from "mixed events" (as described in Section 3) and from the fitting of the M^2 spectra by a linear function. The latter is done in the M^2 range, excluding the proton, deuteron and triton signal windows.
- Systematic uncertainty calculated as half of the difference between the p/d/t yield measured in the ToF-400 and ToF-700 detectors in bins of rapidity y.
- Systematic uncertainty of the event centrality weights estimated 1) from the remaining difference in the shape of the N(track) and N(BD) distributions in y and p_T bins in the data and the simulation; 2) from the difference in the event centrality weights taken from the two-dimensional N(track) / N(BD) distribution relative to the one-dimensional N(BD) distribution.

Table 2 summarizes the mean values, averaged over p_T, y and N_{tr} of the systematic uncertainties of the various factors of Eq. (1), $n_{p,d,t}$, ϵ_{rec}, and ϵ_{trig}. The total systematic uncertainty from these sources, calculated as the square sum of their uncertainties from different sources, is listed in Table 2 for each target.

The luminosity is calculated from the beam flux Φ as given by the beam trigger (see Section 2) and the target thickness l using the relation: $L = \Phi \rho l$ where ρ is the target density expressed in atoms/cm^3. The systematic uncertainty of the luminosity is estimated from the fraction of the beam that can miss the target, determined from the vertex positions, and found to be within 2%. The inelastic cross sections of Ar+C, Al, Cu, Sn, Pb interactions are taken from the predictions of the DCM-SMM model. The σ_{inel} uncertainties for Ar+C, Al, Cu, Sn, Pb interactions are estimated from the empirical formulas taken from ref. [35, 36] and given in Table 1.

7 Rapidity and mean transverse mass spectra

At a kinetic energy of 3.2 GeV/nucleon, the rapidity of the nucleon-nucleon center-of-mass (CM) system is $y_{CM} = 1.08$. The rapidity intervals covered in the present measurements, $0.9 < y < 2.5$, $0.7 < y < 2.3$ and $0.7 < y < 2.1$ for protons, deuterons and tritons, respectively, correspond therefore to the forward and central rapidity regions in the nucleon-nucleon CM system. The measured yields of protons, deuterons and tritons in m_T and y bins in the two centrality intervals in Ar+C,Al,Cu,Sn,Pb interactions can be found in ref. [37].

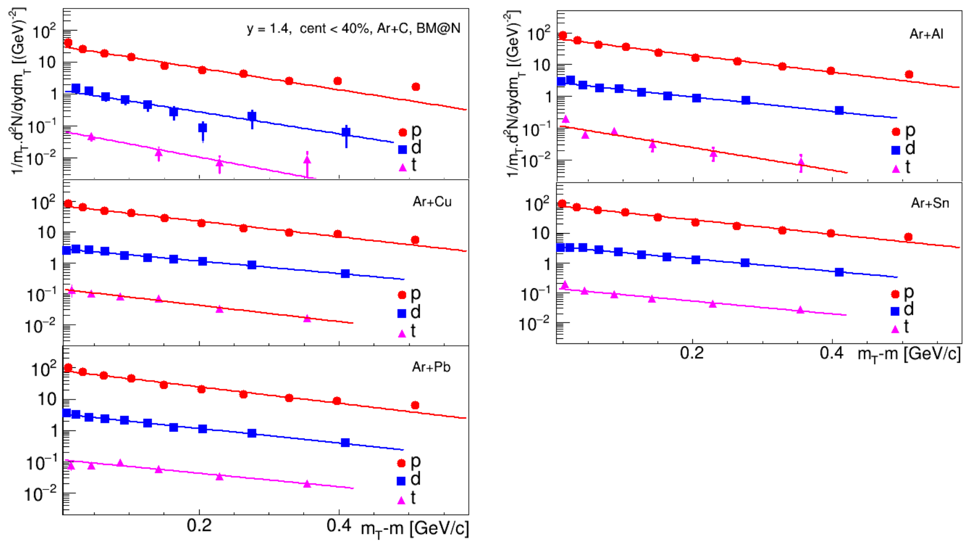

Figure 7: Transverse mass spectra of protons, deuterons, tritons produced at rapidity $y = 1.4$ in Ar+C, Al, Cu, Sn, Pb interactions with centrality 0-40%. The vertical bars and boxes represent the statistical and systematic uncertainties, respectively. The lines show the results of the fit by an exponential function.

As an example, Fig. 7 shows the transverse mass $m_T - m = \sqrt{m_{p,d,t}^2 + p_T^2} - m$ spectra of protons, deuterons and tritons produced in various targets at $y = 1.4$ in the 0-40% centrality class. The spectra are parameterised by an exponential function as:

$$\frac{1}{m_T} d^2N/dydm_T = \frac{dN/dy}{T_0(T_0 + m)} \exp(-(m_T - m)/T_0) \quad (2)$$

where the fitting parameters are the integral of the m_T spectrum, dN/dy, and the inverse slope, T_0. The dN/dy and T_0 values extracted from the fit can be found in ref. [37]. The dN/dy distributions of protons, deuterons and tritons produced in collisions with centrality 0-40% in the various targets are shown in Figs. 8a, 9a and 10a, respectively. The figures show also the comparison of the results with predictions of the DCM-SMM and PHQMD models.

It is seen that the shapes of the particle rapidity density vary strongly with the target mass. For protons, the models have quite similar predictions, which are in reasonable agreement with the experimental results in the forward rapidity range. At mid-rapidity, the models under-estimate the data for interactions with the targets heavier than the carbon; this might indicate that the degree of nuclear

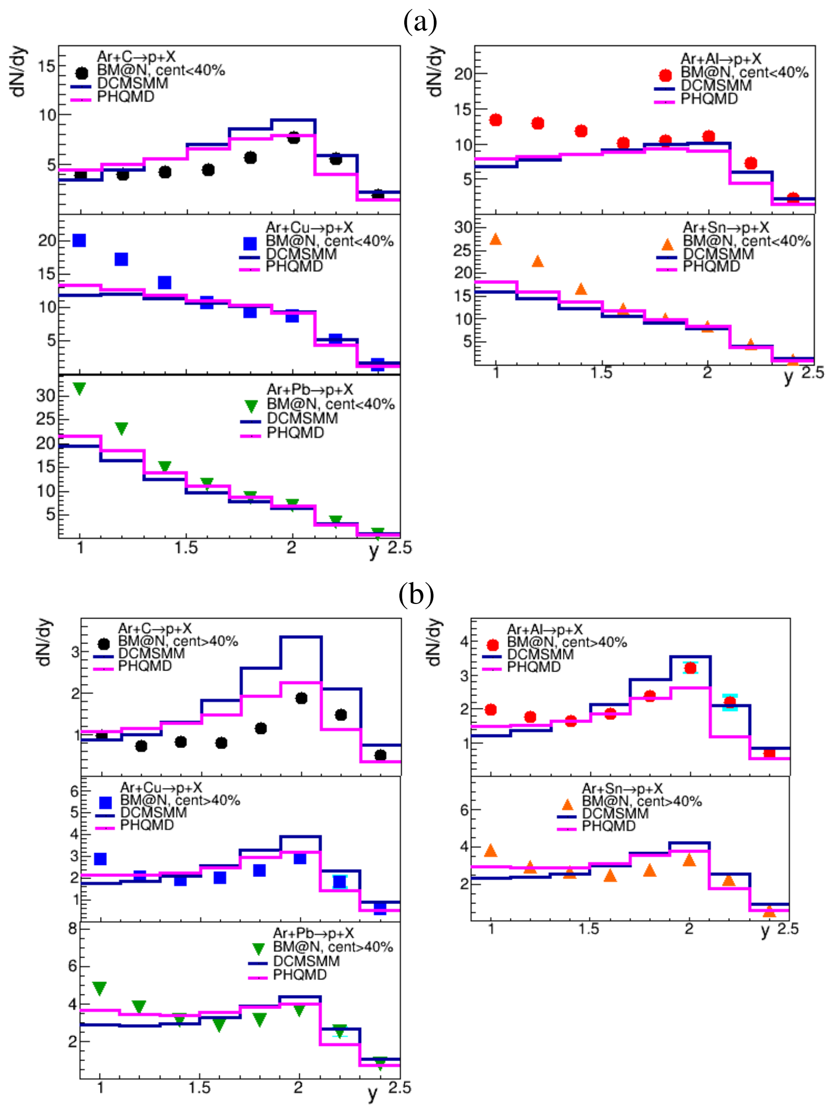

Figure 8: Rapidity distributions dN/dy of protons produced in Ar+C, Al, Cu, Sn, Pb interactions at 3.2A GeV with centrality 0-40% (a) and 40-100% (b). The results are integrated over p_T. The vertical bars and boxes represent the statistical and systematic uncertainties, respectively. The predictions of the DCM-SMM and PHQMD models are shown as blue and magenta lines.

(a)

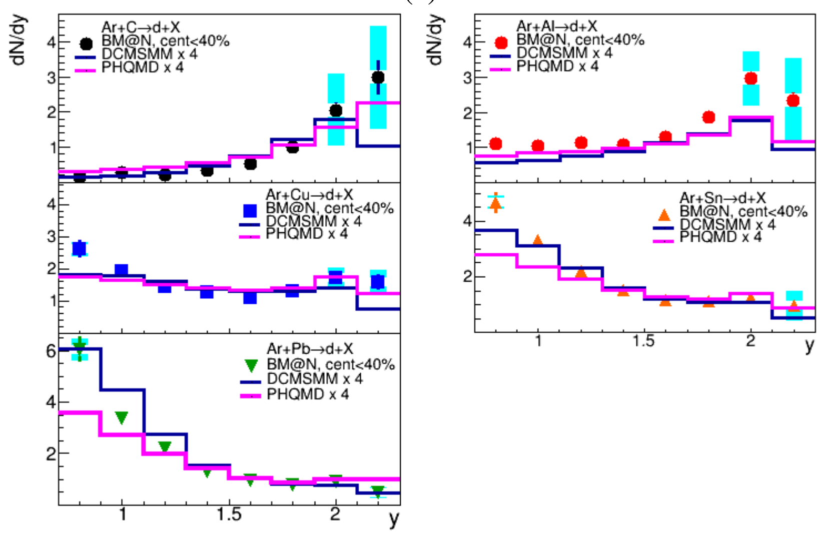

(b)

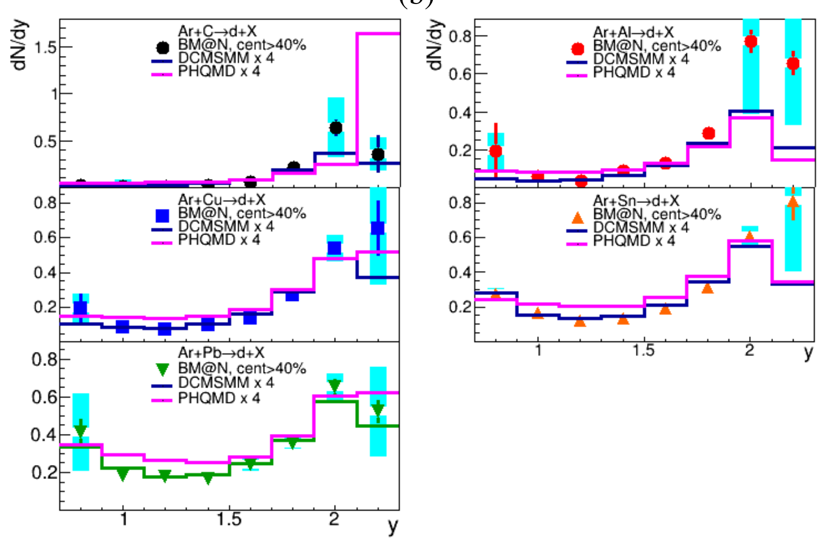

Figure 9: Rapidity distributions dN/dy of deuterons produced in Ar+C,Al, Cu, Sn, Pb interactions with centrality 0-40% (a) and 40-100% (b). The results are integrated over p_T. The vertical bars and boxes represent the statistical and systematic uncertainties, respectively. The predictions of the DCM-SMM and PHQMD models, multiplied by a factor 4, are shown as blue and magenta lines.

(a)

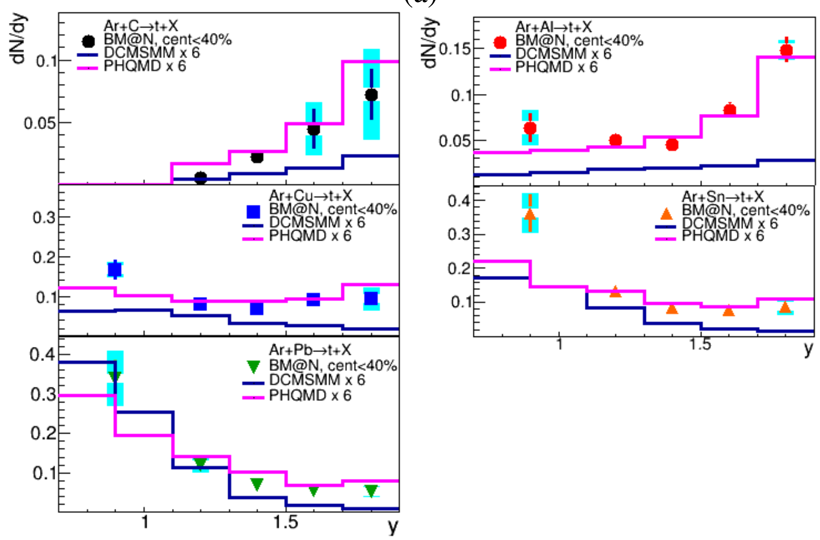

(b)

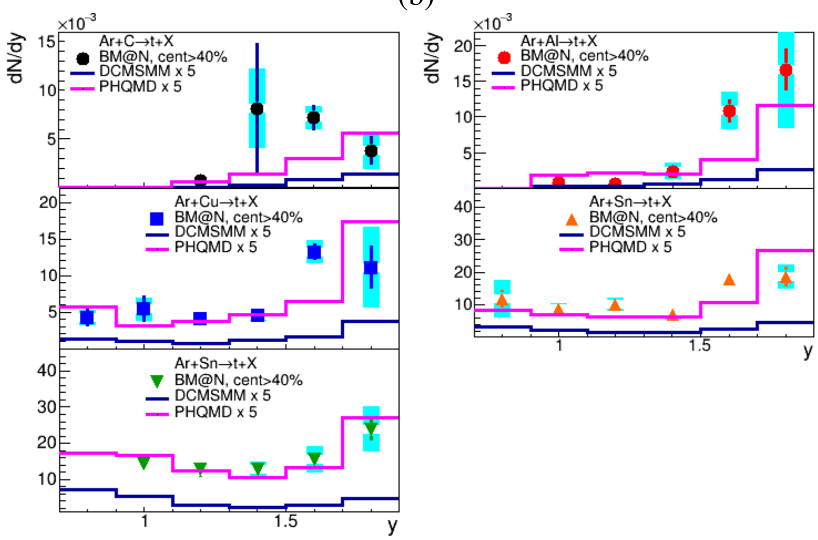

Figure 10: Rapidity distributions dN/dy of tritons produced in Ar+C,Al, Cu, Sn, Pb interactions with centrality 0-40% (a) and 40-100% (b). The results are integrated over p_T. The vertical bars and boxes represent the statistical and systematic uncertainties, respectively. The predictions of the DCM-SMM and PQHMD models, multiplied by factors 6 in (a) and 5 in (b), are shown as blue and magenta lines.

stopping in the data is higher than in the models.

Deuterons and tritons are predominately produced in the beam fragmentation region for Ar+C and Ar+Al interactions, whereas for heavier targets they are mostly produced at mid-rapidity. For deuterons and tritons, the models reasonably describe the shape of the experimental spectra, but under-predict the absolute yields by factors of 4 and 6, respectively.

The dN/dy distributions of protons, deuterons and tritons produced in collisions with centrality 40-100% in the various targets are shown in Figs. 8b, 9b and 10b, respectively. The largest contribution is observed in the beam fragmentation range for all the targets. This tendency is reproduced by the DCM-SMM and PHQMD models, but here also the models under-estimate the absolute yields for deuterons and tritons by factors 4 and 5, respectively. A significant deficit of deuterons and tritons in the PHQMD model relative to the experimental data has also been observed in central (0-10%) collisions of Au+Au at $\sqrt{s}$ of 3 GeV by the STAR experiment [38].

The observed discrepancy between the data and the DCM-SMM and PHQMD models could be due to feed-down from excited nuclear states that is not taken into account in the models. At BM@N collision energies, the reaction zone consists of a hadronic gas that is dominated by nucleons and stable nuclei ($d, t,$^{3}He, ^{4}He). However, in addition to these, there are many excited nuclear states with mass number $A \geqq 4$. The role of the feeddown from these states for the description of light nuclei production in a broad energy range was discussed in ref. [39]. As reported in [39], feeding gives a significant contribution to the yields of d, t at NICA/BM@N energies: as much as 60% of all final tritons and 20% of deuterons may come from the decays of excited nuclear states.

The mean transverse kinetic energy, defined as $\langle E_T \rangle = \langle m_T \rangle - m$, is related to the T_0 value extracted from the fit of the m_T spectrum by the following equation:

$$\langle E_T \rangle = \langle m_T \rangle - m = T_0 + T_0^2/(T_0 + m) \quad (3)$$

The $\langle E_T \rangle$ values of protons in the 0-40% centrality class are shown in Fig. 11a as a function of rapidity. The maximal values of $\langle E_T \rangle$ are measured at rapidity $1.0 < y < 1.3$, i.e. at mid-rapidity in the CM system. In general, the y dependence of $\langle E_T \rangle$ for protons is consistent with predictions of the DCM-SMM and PHQMD models.

The $\langle E_T \rangle$ values for deuterons and tritons in the 0-40% centrality class are shown as a function of rapidity in Figs. 11b and 11c, respectively. PHQMD reproduces the rise of the data at mid-rapidity in CM for deuterons and tritons

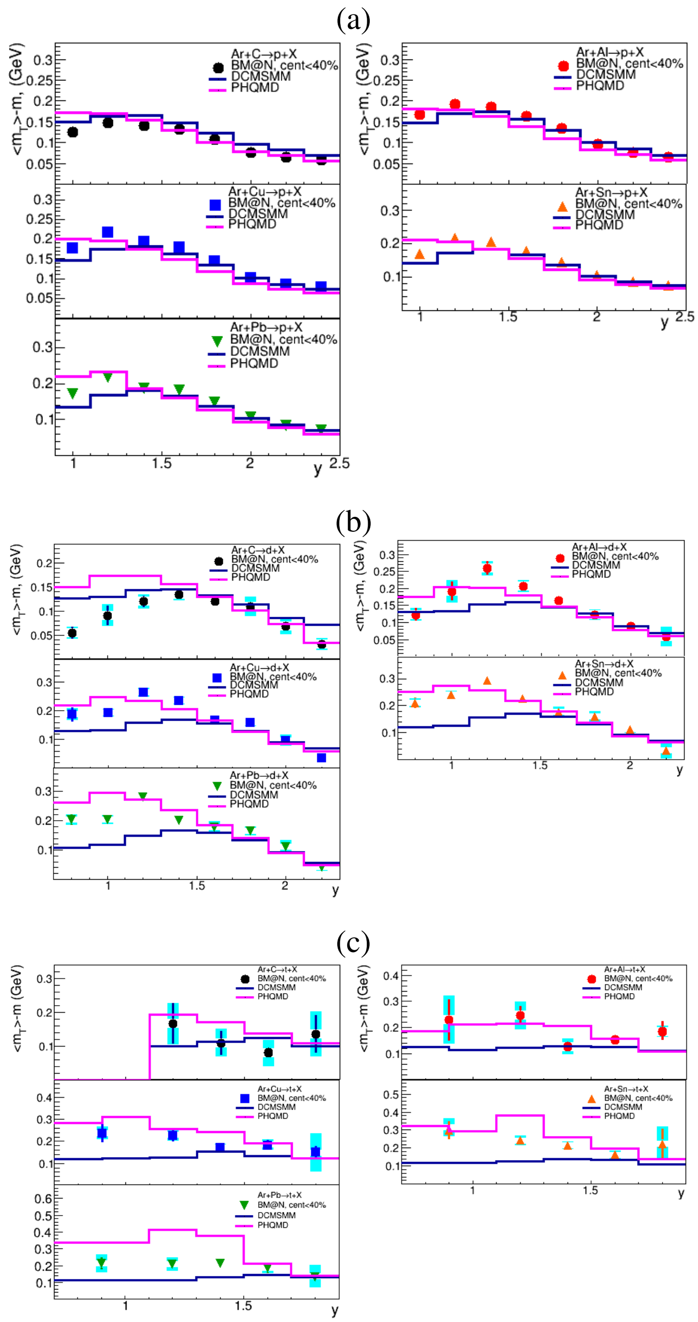

Figure 11: Rapidity y dependence of the mean transverse kinetic energy $\langle E_T \rangle = \langle m_T \rangle - m$ of protons (a), deuterons (b) and tritons (c) in Ar+C, Al, Cu, Sn, Pb interactions with centrality 0-40%. The vertical bars and boxes represent the statistical and systematic uncertainties, respectively. The predictions of the DCM-SMM and PHQMD models are shown as blue and magenta lines.

relative to protons, where as the DCM-SMM model predicts similar $\langle E_T \rangle$ values for protons, deuterons and tritons in contrast with the experimental results.

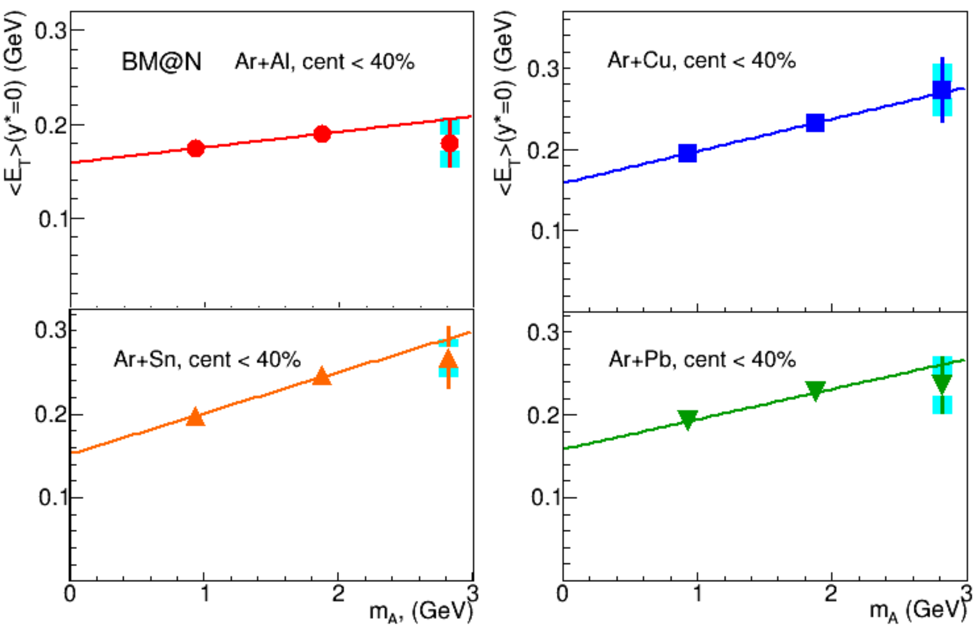

Figure 12: Dependence of the mean transverse kinetic energy $\langle E_T(y^* = 0) \rangle$ on the mass of the nuclear fragment measured in Ar+Al,Cu,Sn,Pb collisions with centrality 0-40%. Linear fits to the data points are indicated by lines.

Figure 12 shows the dependence of the mid-rapidity value of $\langle E_T(y^* = 0) \rangle$ on the mass of the nuclear fragment. The mid-rapidity value of E_T is calculated as the average value over the three points at y=1.0, 1.2 and 1.4. To cross-check the result of this averaging, the rapidity dependence of $\langle E_T \rangle$ for each particle sort in Fig. 11 was fitted with a functional form of the Boltzmann approximation $E_T(0)/\cosh y^*$ with the midrapidity transverse energy $E_T(0)$ being the fit parameter. We found that the difference between $E_T(0)$ and $\langle E_T(y^* = 0) \rangle$ is less than 2%. Figure 12 shows that $\langle E_T(y^* = 0) \rangle$ rises approximately linearly with the mass of the nuclear fragment. For the Ar+C colliding system (not shown) no mass dependence of the $\langle E_T \rangle$ value is observed.

The mean transverse kinetic energy could be expressed as the sum of the energy of radial flow and random thermal motion as [41]:

$$\langle E_T \rangle \approx E_{therm} + E_{flow} = 3/2T^* + (\gamma - 1)m \qquad (4)$$

where $\gamma = 1/\sqrt{1 - \langle\beta\rangle^2}$, $\langle\beta\rangle$ is the average radial collective velocity, T^* is the temperature of the thermal motion, and m is the fragment mass. The parameter T^* obtained from the extrapolation of the linear fits to zero mass, blue shifted, and directly related to the source temperature T as:

$$T^* = T\sqrt{(1 + \langle\beta\rangle)/(1 - \langle\beta\rangle)} \tag{5}$$

The average radial velocity $\langle\beta\rangle$ and source temperature at the kinetic freeze-out extracted from these fits are given in Table 3. One finds a flow velocity consistent with zero in central Ar+C collisions. Nuclear collisions of such small systems can be considered as a superposition of independent nucleon-nucleon interactions, therefore, the density of participants reached in these reactions is probably not high enough to create a fireball with strong collective behavior. In contrast, for larger colliding systems (Ar+Al,Cu,Sn,Pb) the particle density and the re-scattering rate inside the reaction zone are higher, giving rise to a mean expansion velocity. It appears that the observed mass dependence for T and $\langle\beta\rangle$ is weak at BM@N energies: the fits give nearly the same temperature and a slight increase of the flow velocity. This might be an indication that the increase of the reaction volume and the number of collisions with the target mass is not accompanied by a significant compression of the nuclear matter (note also discussion about the degree of nuclear stopping in Section 9).

The BM@N radial flow results could be compared with measurements at lower and higher energies. The FOPI experiment measured $\langle\beta\rangle \sim 0.35$ in Au+Au collisions at 1.2A GeV and found that the radial flow decreases below $\langle\beta\rangle \sim 0.20$ at even lower energies and in interactions of middle-size nuclei [42]. Measurements of the EOS experiment [43] in Au+Au collisions at (0.25-1.15)A GeV are consistent with these results. At higher energies the NA49 [41] ($\sqrt{s_{NN}}$=6-17 GeV) and STAR BES [44, 45] ($\sqrt{s_{NN}}$=7-39 GeV) experiments measured $\langle\beta\rangle \sim 0.45$ in interactions of heavy nuclei (central Pb+Pb and Au+Au). The STAR experiment measured that the $\langle\beta\rangle$ values decrease with decreasing of the colliding system size [45]. The experiments also found that the temperature T increases from ~ 30 MeV to ~ 120 MeV from energies of FOPI to NA49 and STAR BES. The $\langle\beta\rangle$ and T values reported here in argon-nucleus interactions (except for Ar+C) are consistent with the energy and system size trends observed in these experiments.

8 Coalescence factors

Within a coalescence model [18, 19] nuclear fragment formation is characterized by a coalescence factor B_A, defined through the invariant momentum spectra by the equation:

$$E_A d^3N_A/d^3p_A = B_A(E_p d^3N_p/d^3p)^Z(E_n d^3N_n/d^3p)^{A-Z}_{|p=p_A/A}$$

where p_A and $p = p_A/A$ are momenta of the nuclear fragment A and the nucleon, respectively. It relates the yield N_A of nuclear fragments with charge Z and atomic mass number A to the yields of the coalescing nucleons N_p and N_n at the same velocity. Assuming that the neutron momentum density is equal to the proton momentum density at freeze-out, the B_A value can be calculated as:

$$B_A = d^2N_A/2\pi p_{T,A}dp_{T,A}dy/(d^2N_p/2\pi p_T dp_T dy)^A \quad (6)$$

In a thermodynamic approach [46, 47] B_A is inversely related to the fireball volume: $B_A \sim V_{eff}^{1-A}$. In accordance with model expectations [21] strong position-momentum correlations present in the expanding source lead to a higher coalescence probability at larger values of p_T. Assuming a box-like transverse density profile of the source, the model predicts:

$$B_A \propto \exp[m_T(1/T_p - 1/T_A)]/(m_T R_{||}(m_T)R_{\perp}^2(m_T))^{A-1} \quad (7)$$

where $R_{\perp}$ and $R_{||}$ are the femtoscopic radii of the source in the longitudinally co-moving system [21], T_p and T_A are the transverse momentum slopes for proton and nucleus A, respectively.

Figs. 13a and 13b show the B_2 and B_3 values as a function of the transverse momentum measured in argon-nucleus interactions with centrality 0-40%. The

Table 3: T and $\langle\beta\rangle$ values evaluated from the linear fit of the $\langle E_T\rangle = \langle m_T\rangle - m$ values of protons, deuterons and tritons produced in Ar+A interactions with centrality 0-40%. The first error is the statistical uncertainty, the second error is the systematic uncertainty.

	Ar+C	Ar+Al	Ar+Cu	Ar+Sn	Ar+Pb
T , MeV	$90 \pm 3 \pm 3$	$88 \pm 5 \pm 4$	$80 \pm 5 \pm 3$	$74 \pm 5 \pm 4$	$80 \pm 5 \pm 4$
$\langle\beta\rangle$	0.0 ± 0.05 ± 0.01	0.18 ± 0.05 ± 0.02	0.27 ± 0.03 ± 0.02	0.30 ± 0.03 ± 0.02	0.26 ± 0.03 ± 0.02

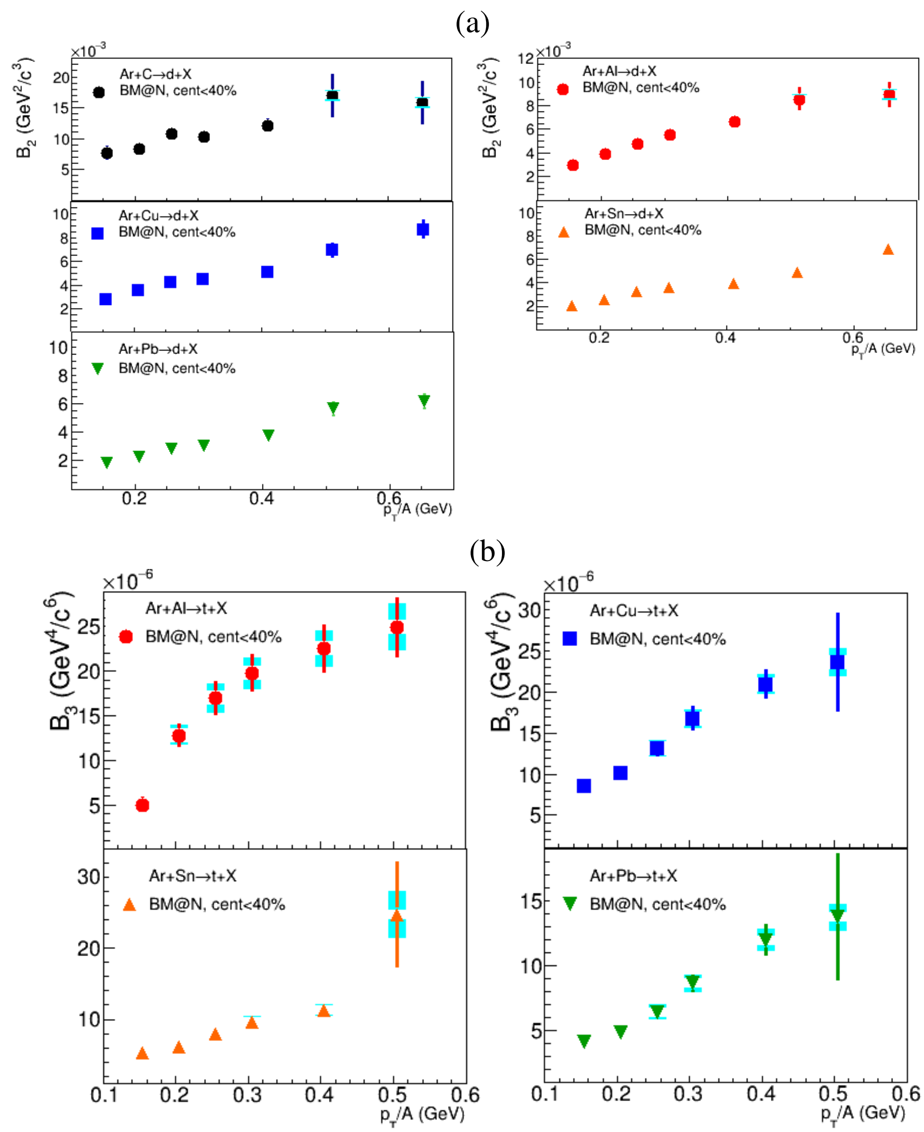

Figure 13: Coalescence parameter B_2 for deuterons (a) and B_3 for tritons (b) measured as a function of p_T/A in Ar+A collisions with centrality 0-40%.

transverse momentum is scaled to the atomic number of the nuclear fragment (deuteron, triton), p_T/A. The yields of protons (N_p), deuterons (N_d) and tritons (N_t) are measured in the same rapidity range, namely $0.9 < y < 1.7(-0.18 < y^* < 0.62)$. The statistics of tritons is not sufficient to present B_3 for Ar+C interactions. It is found, that B_2 and B_3 rise with p_T for all the measured targets, but the dependence is closer to linear rather than exponential. The B_2 and B_3 values at low p_T are smaller for heavier targets compared to lighter targets.

Table 4: Coalescence parameters $B_2(p_T = 0)$ and $B_3(p_T = 0)$ extrapolated to $p_T = 0$ using an exponential fit to $B_2(p_T)$ and $B_3(p_T)$ and coalescence radii $R^d_{coal}(p_T = 0)$ and $R^t_{coal}(p_T = 0)$ evaluated from the $B_2(p_T = 0)$ and $B_3(p_T = 0)$ values for deuterons and tritons produced in Ar+A interactions with centrality 0-40%. The quoted errors are the quadratic sums of the statistical and systematic uncertainties.

	Ar+C	Ar+Al	Ar+Cu	Ar+Sn	Ar+Pb
$B_2(p_T = 0)/10^3$, GeV^2/c^3	5.5 ± 1.9	1.7 ± 0.5	1.8 ± 0.4	1.2 ± 0.4	1.1 ± 0.2
$B_3(p_T = 0)/10^6$, GeV^3/c^4		1.7 ± 1.7	4.0 ± 1.2	2.7 ± 0.6	1.8 ± 0.4
$R_d(p_T = 0)$, fm	2.1 ± 0.3	3.1 ± 0.3	3.0 ± 0.2	3.5 ± 0.4	3.6 ± 0.2
$R_t(p_T = 0)$, fm		3.1 ± 0.5	2.7 ± 0.2	2.9 ± 0.1	3.1 ± 0.1

In order to compare the present measurements of B_2 and B_3 with previously obtained results, the $B_2(p_T)$ and $B_3(p_T)$ values given in Figs. 13a and 13b are extrapolated down to $p_T = 0$ using an exponential fit of the form $B_A(p_T = 0)\exp(a \cdot p_T)$ as predicted by the coalescence model (see equation 7). To evaluate the uncertainty If the fit results with $\chi^2/ndf > 1$ the uncertainty of the parameter $B_A(p_T = 0)$ is scaled up by a factor $\sqrt{\chi^2/ndf}$ following recommendation in ref. [48]. The results of the extrapolation are given in Table 4.

The present results are compared in Fig.14a,b with the measurements of other experiments [41, 49–56]. The B_2 and B_3 results for Ar+A interactions with centrality 0-40% are consistent with the energy dependence of the B_2 and B_3 factors for central interactions of heavy nuclei. It can be seen, that the BM@N measurements follow the general trend of decreasing B_2 and B_3 values with rising collision energy. The B_2 and B_3 values are inversely related to the coalescence

(a)

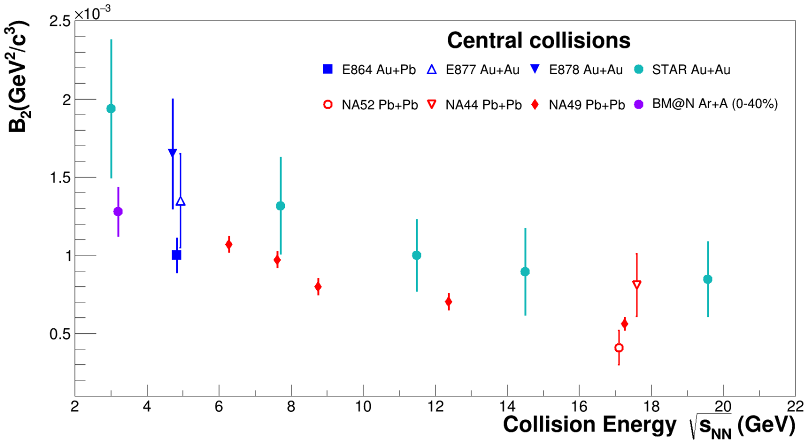

(b)

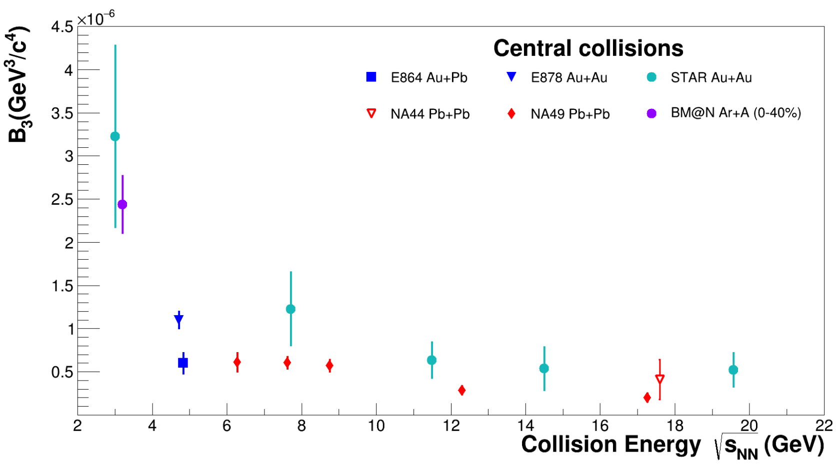

Figure 14: Coalescence parameters $B_2(p_T = 0)$ (a) and $B_3(p_T = 0)$ (b) for deuterons and tritons as a function of the nucleon-nucleon centre-of-mass energy. The BM@N result is the weighed average value calculated for Ar+Al,Cu,Sn,Pb interactions with centrality 0-40%.

radius R_{coal} which is closely related to the femtoscopic radii of the source of produced deuterons and tritons [21]. Using prescriptions in [49] based on [21], the coalescence source radius $R_{coal} = \sqrt[3]{3/2 R_{\parallel} R_{\perp}^2}$ is calculated from the $B_2(p_T = 0)$ and $B_3(p_T = 0)$ values of deuterons and tritons. In the calculations, the C_d and C_t factors from [49] are scaled according to the mass of the colliding systems to account for the suppression related to the increased effective volume due to the finite deuteron and triton radii (see Eq. (4.12) in [21]). The resulting values are in the range of 0.55-0.61 and 0.48-0.53 for C_d and C_t, respectively. The results for R_{coal} are given in Table 4.

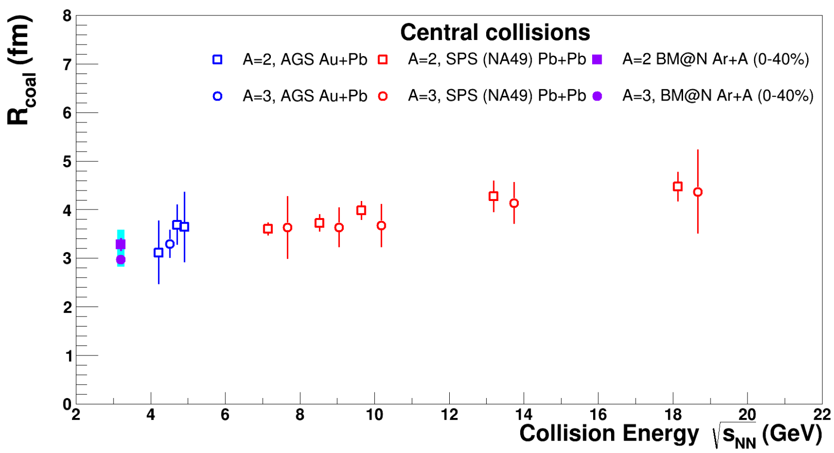

Figure 15: Coalescence radii R_{coal} for deuterons and tritons as a function of the nucleon-nucleon centre-of-mass energy. The BM@N result is the weighed average value calculated for Ar+Al,Cu,Sn,Pb interactions with centrality 0-40%.

The coalescence source radii for deuterons and tritons produced in Ar+Al,Cu, Sn,Pb interactions with centrality 0-40% are consistent with values of 3-3.5 fm except for deuterons produced in Ar+C interactions. The BM@N values for the coalescence radii averaged for Ar+Al,Cu,Sn,Pb interactions are compared in Fig.15 with results at higher energies and larger collision systems as compiled in [41]. Figure 15 exhibits a weak increase of the coalescence radii as a function of the center-of-mass energy in the nucleon-nucleon system. The results reported here also indicate no dependence of the coalescence radii with the system size within the experimental uncertainties.

9 Baryon rapidity distributions, stopping and rapidity loss in Ar+A

The total baryon number in Ar+A collisions at NICA/BM@N energies is basically determined by the nucleons and the light nuclei (d, t,^{3}He). According to the results on the rapidity spectra of protons and light nuclei, presented in Section 7, the number of nucleons bound in clusters contribute to the total number of baryons up to about 15% and 25% in central Ar+C and Ar+Pb reactions, respectively. To obtain the baryon rapidity distribution, we add up the baryon number of the measured protons, deuterons and tritons in every rapidity bin. The obtained distribution is then corrected for unmeasured baryons: neutrons, hyperons and ^{3}He nuclei. Calculations with the PHQMD and UrQMD models indicate that for all collision systems the n/p-ratio is of about 1.1 in the forward hemisphere varying slowly with rapidity and then increasing abruptly to ≈1.22 (the n/p-ratio in the projectile Ar-nucleus) at the beam rapidity. We use these model predictions to estimate the yield of neutrons n, furthermore, we assume that the $t/^3$He ratio is equal to n/p. Hyperons contribute less than 2% to the total baryon number according to the PHQMD and UrQMD [59] models and are thus neglected. The total number of baryons B in a rapidity bin is then calculated as

$$B = p + n + 2.0 \cdot d + 5.7 \cdot t,$$

where the coefficient in front of t is 5.7 = 3.0 (for tritons) + 3.0/1.1 (for ^{3}He).

The resulting baryon rapidity distributions for Ar+Cu collisions are shown in Fig. 16 as a function of the center-of-mass rapidity: the left panel shows the results for 0-40% central collisions, and the right one is for peripheral collisions. As one can see, more baryons are transported to midrapidity in the more central collisions leading to a dramatic difference in the shapes of the dn/dy distributions. To describe those shapes, we fitted the measurements to a 3^{rd} order polynomial in y^2 (as suggested in ref. [57]), and the fit results are shown in Fig. 16 by solid curves.

The average rapidity loss is calculated as

$$\langle \delta y \rangle = y_b - \langle y \rangle, \tag{8}$$

where $y_b = 1.08$ is the rapidity of the projectile in the center-of-mass system, and

$$\langle y \rangle = \int_{y_0}^{y_b} y \frac{dn}{dy} dy \bigg/ \int_{y_0}^{y_b} \frac{dn}{dy} dy \tag{9}$$

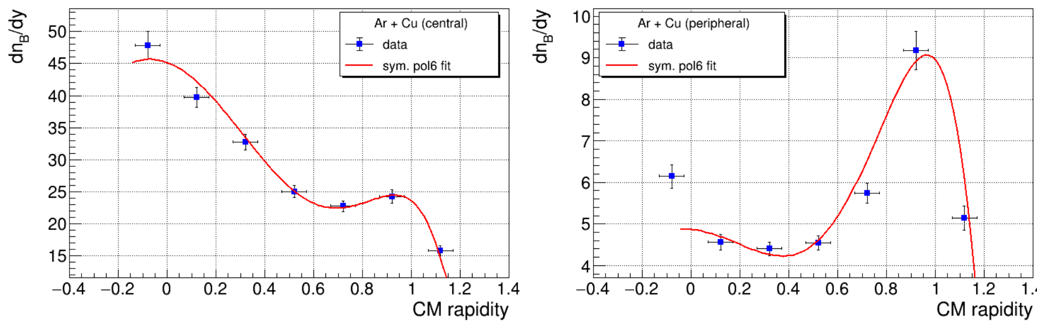

Figure 16: Left: Rapidity distribution of baryons in 0-40% central Ar+Cu collisions. The measurements are shown by solid dots, whereas the solid line is the results of a fit to a 3^{rd} order polynomial in y^2. Right: same for peripheral Ar+Cu collisions.

Table 5: The average rapidity loss $\langle \delta y \rangle$ in Ar+A reactions. The quoted uncertainties are statistical errors.

	Ar+C	Ar+Al	Ar+Cu	Ar+Sn	Ar+Pb
0-40%	0.47 ± 0.03	0.54 ± 0.03	0.60 ± 0.03	0.62 ± 0.04	0.64 ± 0.04
>40%	0.39 ± 0.03	0.42 ± 0.03	0.47 ± 0.03	0.53 ± 0.04	0.55 ± 0.04

This equation refers to net-baryons, i.e. baryons minus antibaryons. At NICA energies, however, the production of antibaryons is so small that the difference between baryons and net-baryons is negligible. The low integration limit in Eq. 9 is the midrapidity ($y_0 = 0$), but, the calculation result is correct only for a little mixing of projectile and target participants. For the asymmetric Ar+A collisions, considered here, we follow the suggestion from ref. [58] and define y_0 such that the area enclosed by the baryon dn/dy across the bounding values is equal to the number of participating nucleons in the projectile N_p^{proj}. These numbers of participants were determined by averaging the results of the UrQMD and DCM-SMM models. The y_0 value varies from 0.12 for Ar+Pb to -0.3 for Ar+C collisions.

The final $\langle \delta y \rangle$ values for central and peripheral collisions are listed in Table 5. A clear trend is observed: $\langle \delta y \rangle$ increases with the target mass and with centrality. This behavior is expected because the probability of multiple interactions in the projectile-target overlap region also rises with centrality and target mass. The quoted uncertainties (statistical errors) are the standard errors of the mean $\langle y \rangle$ calculated from the data points within the rapidity range [$y_0 - y_b$]. The systematic error in determining the rapidity loss values come from the uncertainty in the fitting procedure used to describe the baryon rapidity spectra, and poor knowledge of the number of participants in the projectile N_p^{proj} used in defining the low limit integration y_0 in Eq. 9. The uncertainty related to the fitting procedure is taken as the difference between the total baryon number estimated from the fit function and the one obtained from data points. The uncertainty associated with poor knowledge of N_p^{proj} is estimated by considering the predictions from two different models, UrQMD and DCM-SMM. The overall systematic error in $\langle \delta y \rangle$ varies from 7% to 12%.

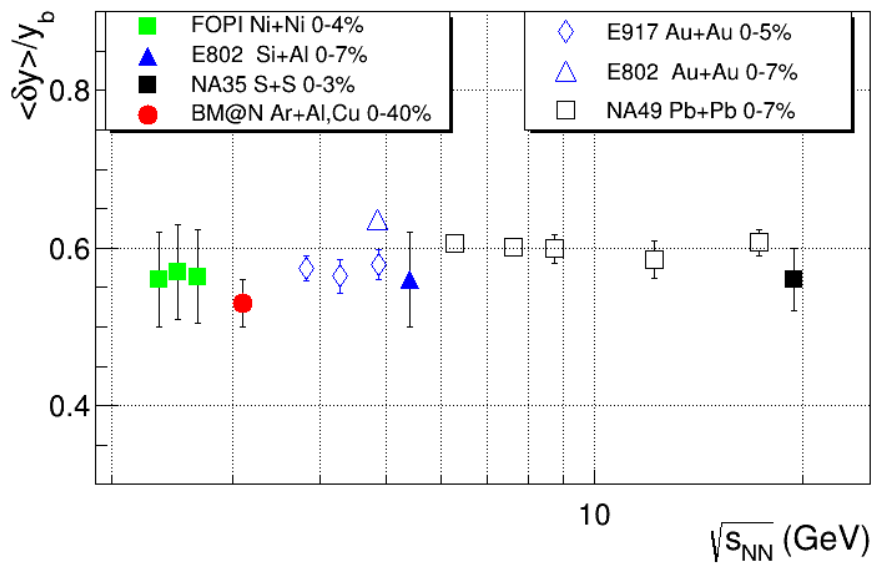

Figure 17: The excitation function of the scaled average rapidity loss $\langle \delta y \rangle / y_b$ in nucleus-nucleus collisions. Medium-size colliding systems [58, 60, 61] are drawn by solid symbols, while heavy systems [58, 62, 63] are shown by open ones. Centrality intervals are indicated in the legends. The BM@N data point is the average of Ar+Al and Ar+Cu results.

Figure 17 shows the energy dependence of the scaled average rapidity shift $\langle \delta y \rangle / y_b$ in nucleus-nucleus collisions as a function of $\sqrt{s_{NN}}$. The average of the BM@N results obtained in Ar+Al and Ar+Cu collisions is shown together with results from medium-size almost symmetric colliding systems from [58, 60, 61] (solid symbols) and those from heavy colliding systems [58, 62, 63] (open symbols). The corresponding centrality intervals are indicated in the legends. As one can see, the scaled rapidity loss does not vary over a broad energy range.

10 Particle ratios

The rapidity and system size dependence of the deuteron-to-proton ratio R_{dp} in Ar+A collisions at $\sqrt{s_{NN}} = 3.1$ GeV is presented in Fig. 18, a)-e). As one can see, R_{dp} rises strongly from midrapidity to the beam rapidity in peripheral collisions. The same trend is observed in central Ar+C collisions. In contrast, in central collisions of argon nuclei with targets heavier than (or equal to) aluminum, R_{dp} indicates a plateau-like behavior near midrapidity followed by an increase toward the beam rapidity region. The plateau region for R_{dp} increases gradually with the target mass number covering almost all the measured rapidity range in Ar+Pb collisions.

The midrapidity R_{dp} values from central and peripheral Ar+A collisions as a function of the midrapidity baryon density dn_B/dy (obtained from the fits of Fig. 16) are presented in Fig. 18, f). As one can see, R_{dp} increases steadily for small values of dn_B/dy and then levels off at higher values.

For a system in chemical equilibrium and if the size of the emitting source is larger than the width of the deuteron wave function, the ratio of the invariant yield of deuterons to the one of protons can be related to the average proton phase-space density at the freezeout $\langle f_p \rangle$ as

$$\langle f_p \rangle = \frac{R_{pn}}{3} \frac{E_d \frac{d^3 N_d}{d^3 P}}{E_p \frac{d^3 N_p}{d^3 p}} \tag{10}$$

where R_{pn} is the proton-to-neutron ratio, $P = 2p$, and the factor of 3 accounts for the spins of the particles [13]. The $\langle f_p \rangle$ value depends on the strength of nuclear stopping in the reaction as well as on the outward flow effects. Figure 19 shows the evolution of the average proton's phase-space density as a function of transverse momentum. Here, the ratio of deuterons to protons is obtained in the rapidity range $0.05 < y < 0.45$ and at three p_T/A values: 0.15, 0.3, and 0.45 GeV/c; the $\langle f_p \rangle$ values are calculated according to Eq. 10. The values of the R_{pn} ratio in the chosen phase-space region were taken from the UrQMD model. Some data points in the figure are displaced along the x-axis for clarity. In a thermal source at a low phase-space density ($f << 1$) $\langle f_p \rangle$ follows a Bolzmann distribution and decreases exponentially with p_T [64]. If, however, outward flow is present in the system, $f(p_T)$ may become flatter [65]. Taking into account the results on the radial velocity and temperature presented in Table 3 (i.e. almost no radial expansion in Ar+C and approximately the same values of T and β in Ar+Al,Cu,Sn,Pb), one can conclude that the observed trend in Fig 19 is indeed consistent with the

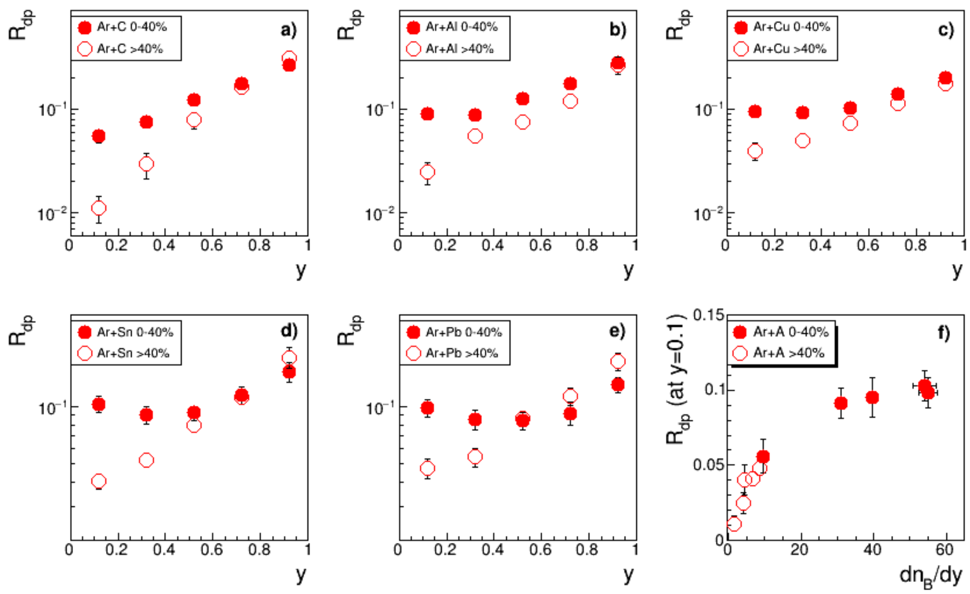

Figure 18: R_{dp} as a function of center-of-mass rapidity y in Ar+C (a), Ar+Al (b), Ar+Cu (c), Ar+Sn (d), and Ar+Pb (e) collisions. Central and peripheral collisions are shown by solid and open symbols, respectively. f): Midrapidity R_{dp} as a function of midrapidity baryon density dn_B/dy in Ar+A collisions.

.

expectations.

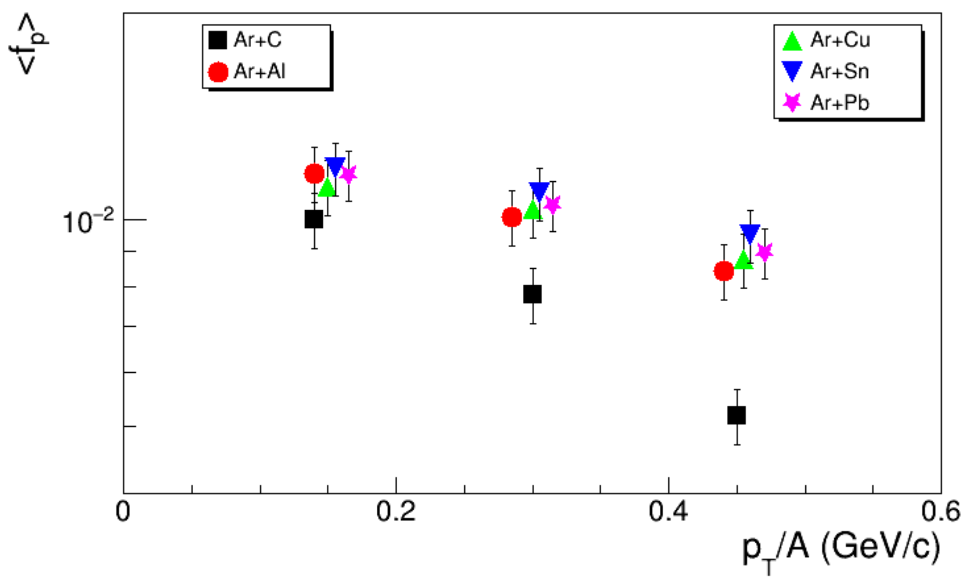

Figure 19: Average proton phase-space density for central Ar+A collisions as a function of p_T/A within the rapidity range 0.05< y <0.45. The results are obtained at $p_T = 0.15, 0.3, 0.45$ GeV/c, but displaced horizontally for clarity.

It was identified long time ago that the nuclear cluster abundances and the entropy value attained in the collisions are related. According to early investigations [66], in a mixture of nucleons and deuterons in thermal and chemical equilibrium the entropy per nucleon S_N/A can be deduced from the deuteron-to-proton ratio R_{dp} as

$$\frac{S_N}{A} = 3.945 - \ln R_{dp} - \frac{1.25 R_{dp}}{1 + R_{dp}} \tag{11}$$

Furthermore, as the collision energy increases, the contribution of mesons S_π to the total entropy becomes important. Following [67], the entropy of pions per nucleon can be estimated by

$$\frac{S_\pi}{A} = 4.1 \frac{N_\pi}{N_N}, \tag{12}$$

where $N_N = N_p + N_n$ is the total number of nucleons.

We thus calculated the total entropy S/A near midrapidity as the sum of the nucleon and pion entropy contributions according to Eq. 11 and Eq. 12. To estimate S_π, we used the recently published BM@N results on positively charged pions [8], while the contribution of π^-, π^0, and neutrons was obtained from the UrQMD model. We found that the contribution of pions to the total entropy does not exceed 25% in Ar+A collisions at NICA energies. Finally, S/A is found to be 10.6, 8.0, 8.0, 7.9, and 8.0 in central Ar+C, Ar+Al, Ar+Cu, Ar+Sn, and Ar+Pb, respectively. The estimated uncertainty in S/A is about 15%. In Fig. 20 we present the energy dependence of S/A in central heavy-ion collisions. This compilation includes data from experiments that have published numerical values for the midrapidity yields of charged pions, protons, and light nuclei [41, 60, 68–72]. In this figure, we show the BM@N 'saturation' S/A-value of 8.0. As can be seen from the figure, the total entropy increases steadily with collision energy.

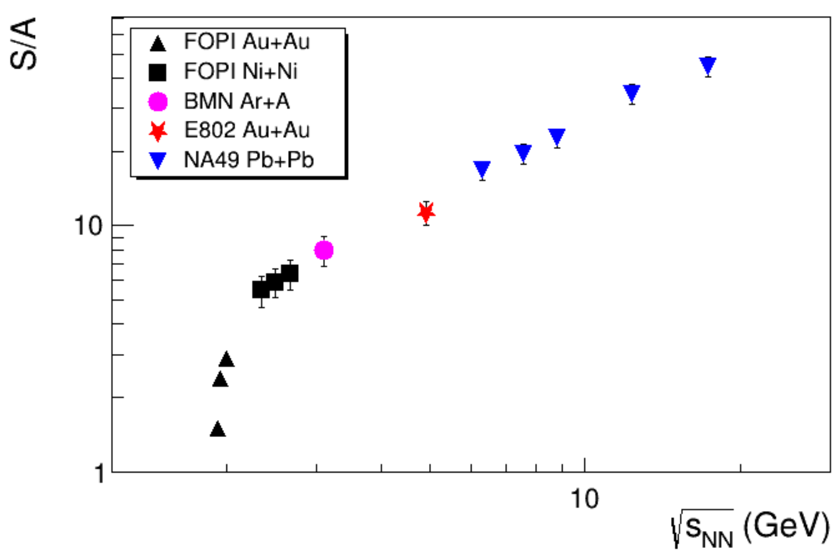

Figure 20: The excitation function of the entropy per baryon S/A from SIS/FOPI [60, 68], AGS/E802 [69], SPS/NA49 [41, 70–72] and NICA/BM@N (this study).

It has been established experimentally that the cluster production yields scaled by the spin degeneracy factor (2J+1) decrease exponentially with the atomic mass number A [41, 73]. As an example, Fig. 21 (left panel) presents dn/dy/(2J+1) at midrapidity for p, d, t as a function of A from 0-40% central Ar+Sn collisions. The particle rapidity density values are extracted from the fits of Fig. 7. The A-

dependence of the yields was fitted to a form:

$$\frac{dn}{dy}(A) = const/p^{A-1}, \tag{13}$$

where the parameter p ('penalty factor') determines the penalty of adding one extra nucleon to the system.

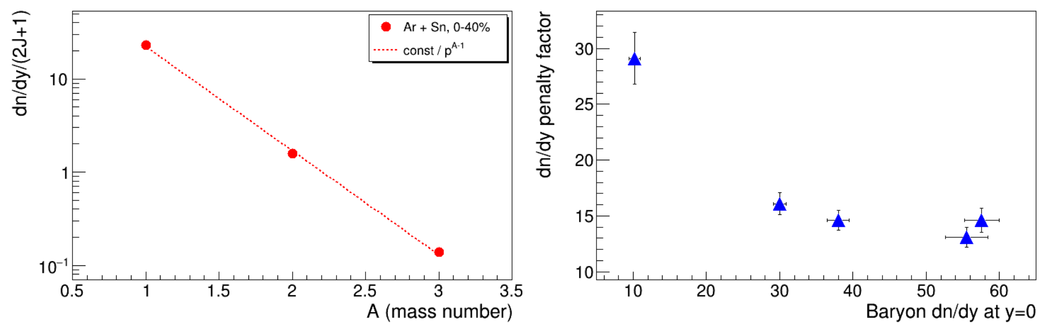

Figure 21: Left: Midrapidity dn/dy/(2J+1) for p, d, t from central Ar+Sn collisions. The dashed line is a fit to Eq. 13. Right: Penalty factor from central Ar+A collisions versus baryon rapidity density at $y = 0$.

The penalty factor is sensitive to the nucleon density attained in the reaction (the larger the density the smaller the penalty). The p-factors from central Ar+A collisions are listed in Table 6 and shown in Fig. 21 (right panel) as a function of the midrapidity baryon density. The quoted errors are the statistical ones and obtained from the fit to Eq. 13. A clear trend is observed : p decreases for the small baryon densities reached in Ar+C and Ar+Al reactions and then saturates above dn/d$y \approx 30$.

In the framework of a statistical approach, the penalty factor is determined as:

$$p = e^{(m-\mu_B)/T}, \tag{14}$$

where μ_B, T, and m being the baryochemical potential, freezeout temperature, and nucleon mass, respectively [15]. Equation 14 can be used to determine the source thermodynamic freeze-out parameters T and μ_B as an alternative approach instead of the standard method based on the analysis of hadron abundances in the framework of a thermal statistical model [74]. As reported in ref. [75], the values of kinetic and chemical freeze-out temperatures are similar in heavy-ion collisions below $\sqrt{s_{NN}} = 5$ GeV. Thus, we can use the value of T obtained in the analysis

Table 6: Penalty factor p, temperature T (from Table 3), and baryochemical potential μ_B in 0-40% central Ar+A collisions. The quoted uncertainty is the quadratic sum of the statistical and systematic errors.

Reaction	p	T (MeV)	μ_B(MeV)
Ar+C	29.1 ± 2.3	89.8 ± 4.2	635.3 ± 15.8
Ar+Al	16.1 ± 1.0	88.1 ± 6.4	693.2 ± 18.6
Ar+Cu	14.6 ± 0.7	79.9 ± 5.8	723.8 ± 16.0
Ar+Sn	13.1 ± 0.7	74.3 ± 6.4	746.9 ± 16.9
Ar+Pb	14.6 ± 0.8	80.5 ± 6.4	722.2 ± 17.7

of transverse mass spectra of particles and listed in Table 3 as an estimate for a 'universal' freeze-out temperature. Re-arranging Eq. 14, one can write a formula for μ_B as

$$\mu_B = m - T \ln p \tag{15}$$

The resulting (T, μ_B) freeze-out parameters for central Ar+A collisions are tabulated in Table 6 and shown in Fig. 22. The quoted error is the quadratic sum of the statistical and systematic uncertainties. The BM@N results from medium-size Ar+A collisions follow the trend defined by world data and described by the parameterization from ref. [74] (which is shown by the dashed line) with the only exception of the Ar+C system that is probably too small to obtain a globally equilibrated fireball.

Recently, the STAR experiment reported measurements of the compound yield ratio $R_{ptd} = N_p N_t / N_d^2$ of protons (N_p) and tritons (N_t) to deuterons (N_d) [54]. Coalescence models predict [76] that a non-monotonic behaviour of the ratio as a function of the system size or collision energy is a signature of the neutron density fluctuations Δn: $R_{ptd} \approx g(1 + \Delta n)$ with a color factor $g \simeq 0.29$. Following this argument, R_{ptd} is a promising observable to search for the critical point and/or a first-order phase transition in heavy-ion collisions [77]. In coalescence models, the compound yield ratio should increase as the size of the system decreases. Indeed, this effect is observed by the STAR experiment [55].

To evaluate the R_{ptd} ratio, mean values of the dN/dy distributions for protons, deuterons and tritons are calculated in the rapidity range $0.9 < y < 1.7$ ($-0.18 < y^* < 0.62$). The results are given in Table 7 for argon-nucleus interactions with centrality 0-40%. The quoted error is the quadratic sum of the statistical and systematic uncertainties. No significant variation of the $N_p N_t / N_d^2$ values is observed with the various targets. Taking the differences as a system-

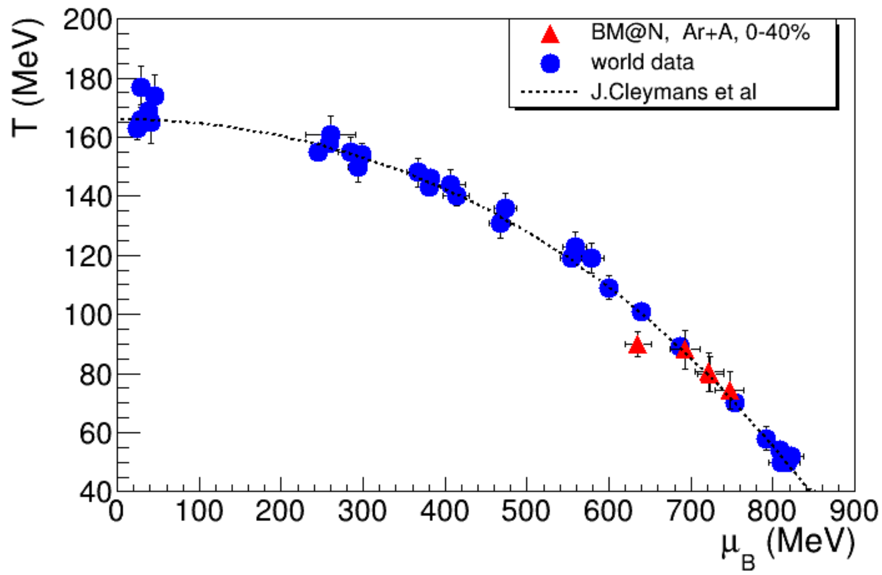

Figure 22: Freeze-out (T, μ_B) parameters for A+A collisions. BM@N results are from this study, world data and the parameterization for the freezeout line (dashed line) are from [74].

.

Table 7: N_pN_t/N_d^2 values evaluated from the mean dN/dy values of protons, deuterons and tritons over the rapidity range $-0.18 < y^* < 0.62$ in Ar+A interactions with centrality 0-40%. The quoted errors are the quadratic sums of the statistical and systematic uncertainties.

	Ar+C	Ar+Al	Ar+Cu	Ar+Sn	Ar+Pb
N_pN_t/N_d^2	0.53 ± 0.10	0.55 ± 0.09	0.69 ± 0.11	0.60 ± 0.07	0.59 ± 0.06

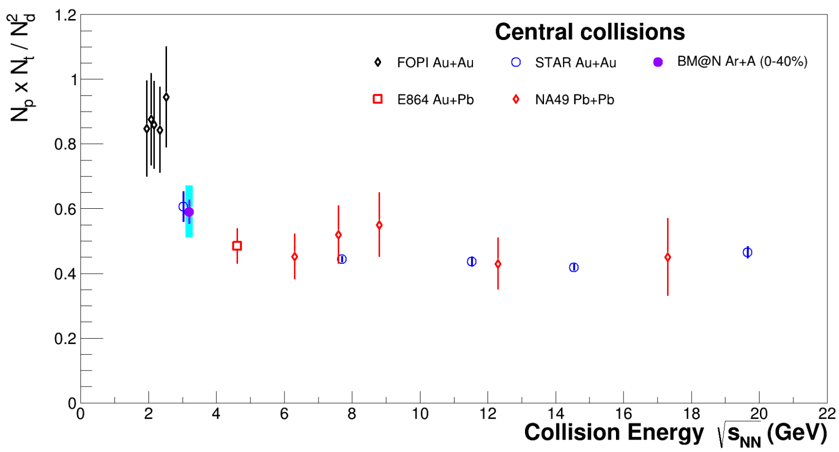

Figure 23: Compound yield ratio $N_p \cdot N_t/N_d^2$ of protons (N_p) and tritons (N_t) to deuterons (N_d^2) as a function of the centre-mass energy of nucleus-nucleus interactions. The BM@N result is the weighed average value calculated for Ar+Al,Cu,Sn,Pb interactions with centrality 0-40%.

atic uncertainty, the weighted average value of the compound ratio is estimated to be 0.59 ± 0.09, where the uncertainty is the quadratic sum of the statistical and systematic uncertainties. Within the uncertainties there is no dependence of the R_{ptd} ratio on rapidity in the measured rapidity range. The BM@N value for R_{ptd} is compared in Fig. 23 with the measurements of other experiments. The BM@N result lays between the values of 0.8-1.0 derived by the FOPI experiment [42] at lower energies and the values of 0.4-0.5 obtained by the E864, STAR and NA49 experiments at higher CM energies $\sqrt{s}$ from 4.3 to 18 GeV [41, 50, 55, 78]. The BM@N value for R_{ptd} is consistent with the STAR Au+Au result measured in the fixed target mode at $\sqrt{s}$ of 3 GeV [56].

11 Summary

First physics results of the BM@N experiment are presented on the proton, deuteron and triton yields and their ratios in argon-nucleus interactions at the beam kinetic energy of 3.2 AGeV. The results are compared with the DCM-SMM and PHQMD models and with previously published results of other experiments.

The transverse mass m_T spectra are measured and the mean transverse kinetic energy $\langle m_T \rangle - m$ are presented for more central 0-40% events as functions of the rapidity y and mass m of the nuclear fragment. The $\langle m_T \rangle - m$ values are found to depend linearly on the mass m. The source temperature at kinetic freeze-out and the average radial velocity are extracted.

The rapidity density dN/dy of protons, deuterons and tritons are presented for the whole p_T range in two centrality ranges. The DCM-SMM and PHQMD models reproduce the shapes of the spectra, but underestimate the deuteron and triton yields by factors four and six, respectively.

The average rapidity loss $\langle \delta y \rangle$ increases with the target mass and with the collision centrality. In contrast, the rapidity loss scaled to the beam rapidity $\langle \delta y \rangle / y_b$ in almost symmetric heavy-ion collisions does not vary over a broad energy range.

The ratio of deuterons to protons R_{dp} rises in peripheral collisions and levels off in central ones, possibly indicating a saturation of the nucleon phase-space density at freezeout. The entropy per baryon S/A was estimated to be $S/A \approx 8$ nicely fitting in the trend of the S/A energy dependence established from other experimental results.

The freezeout fireball parameters T obtained from the transverse mass spectra and the baryo-chemical potential μ_B derived from a coalescence analysis were found to follow the trend of the world T, μ_B values obtained from a statistical analysis of particle abundances.

The deuteron to proton and triton to proton yield ratios are used to calculate the coalescence parameters B_2 and B_3 for deuterons and tritons. The coalescence radii of the deuteron and triton source are extracted from the B_2 and B_3 values extrapolated to $p_T = 0$ and compared with results of other experiments. The compound yield ratio $N_p N_t / N_d^2$ of protons and tritons to deuterons is evaluated and compared with other measurements at lower and higher energies. The results follow the general trend of decreasing values of B_2, B_3 and $N_p N_t / N_d^2$ ratio with increasing energy.

Acknowledgments. The BM@N Collaboration acknowledges the efforts of the staff of the accelerator division of the Laboratory of High Energy Physics at JINR that made this experiment possible. The BM@N Collaboration acknowledges support of the HybriLIT of JINR for the provided computational resources.

References

[1] B. Friman, W. Nörenberg, and V.D. Toneev, Eur. Phys. J. A 3 (1998).

[2] J. Randrup and J. Cleymans, Phys. Rev. C 74 (2006) 047901.

[3] Ch. Fuchs, Prog. Part. Nucl. Phys. 56 (2006) 1-103.

[4] NICA White Paper, Eur. Phys. J. A 52 (2016).

[5] BM@N Conceptual Design Report: http://nica.jinr.ru/files/BM@N/BMN_CDR.pdf

[6] M. Kapishin (for the BM@N Collaboration), Nucl. Phys. A 982 (2019) 967-970.

[7] M. Kapishin (for the BM@N Collaboration), SQM 2019 proceedings, 285 Springer Proc. Phys. 250 (2020) 21-27.

[8] S.Afanasiev et al. (BM@N Collaboration), JHEP 07 (2023) 174.

[9] W. Busza and A. S. Goldhaber, Phys. Lett. 139B, 235 (1984).

[10] G.C. Rossi and G. Veneziano, Phys. Rep. 63 (1980) 153.

[11] A. Capella and B. Z. Kopeliovich, Phys. Lett. B 381, 325 (1996)

[12] D. Kharzeev, Phys. Lett. B 378, 238 (1996)

[13] M.Murray and B. Holzer, Phys Rev. C 63, 054901 (2000).

[14] A. Andronic, P. Braun-Munzinger, and J. Stachel, Phys. Lett. B 673, 142 (2009).

[15] T.A. Armstrong et al (E864 Collaboration) Phys. Rev. Lett. 83, 5431 (1999).

[16] G. Bertsch and J. Cugnon, Phys. Rev. C 24, 2514 (1981).

[17] J. I. Kapusta, Phys. Rev. C 24, 2545 (1981).

[18] S.T. Butler and C.A. Pearson, Phys. Rev. 129, 836 (1963).

[19] A. Schwarzschild and C. Zupancic, Phys. Rev. 129, 854 (1963).

[20] S. Mrowczynski, Phys. Lett. B 277, 43 (1992).

[21] R. Scheibl and U. Heinz, Phys. Rev. C 59, 1585 (1999).

[22] N. Amelin, K. Gudima, and V. Toneev, Sov. J. Nucl. Phys. 51, 1093 (1990).

[23] M. Baznat, A. Botvina, G. Musulmanbekov, V. Toneev, V. Zhezher, Phys. Part. Nucl. Lett. 17 (2020) no. 3; arXiv: 1912.09277v.

[24] J.Aichelin, E. Bratkovskaya et al, Phys. Rev. C 101, 044905 (2020)

[25] BM@N project:
https://bmn.jinr.ru/detector/project/BMN_project.pdf

[26] S. Afanasiev et al., arXiv:2312.17573 [hep-ex]

[27] D. Baranov et al., JINST 12 (2017) no. 06, C06041

[28] V. Babkin et al., Nucl. Instrum. Meth. A 824, P.490-492 (2016); V. Babkin et al., Proceedings of Science, 2014, Vol.213 (Proceedings of TIPP-2014), P.289.

[29] N. Kuzmin et al., Nucl. Instrum. Meth. A 916, P. 190-194 (2019).

[30] K. Alishina et al., Phys. Part. Nucl., 53 (2022) no. 2, 470-475.

[31] V. Akishina and I. Kisel, J. Phys.: Conf. Ser. 599, 012024 (2015), I. Kisel, Nucl. Instrum. Meth. A 566, 85 (2006).

[32] CERN Program Library, Long Writeup W5013, Geneva, CERN, 1993.

[33] https://git.jinr.ru/nica/bmnroot

[34] V.Plotnikov, L.Kovachev, A.Zinchenko, Phys. Part. Nuclei Lett. 20 (2023), 1392–1402

[35] K.Kanaki, PhD Thesis, Technische Universität Dresden, 2007.

[36] H.Angelov et al., P1-80-473, JINR, Dubna.

[37] BM@N web-page:
https://bmn.jinr.ru/wp-content/uploads/2023/07/PiKpaper_TabRes_v3.pdf

[38] STAR Collaboration: [nucl-ex] arXiv:2311.11020

[39] V.Vovchenko et al, Phys. Lett. B 809 (2020) 135746

[40] D.R. Tilley, H.R. Weller, G.M. Hale, Nucl. Phys. A 541 (1992) 1

[41] T.Anticic et al. (NA49 Collaboration) Phys. Rev. C 94, 044906 (2016)

[42] W.Reisdorf et al. (FOPI Collaboration) Nucl.Phys.A 848 (2010) 366-427

[43] M.A.Lisa et al. (EOS Collaboration) Phys.Rev.Lett.75 (1995) 2662

[44] L.Kumar (for the STAR Collaboration), Nucl. Phys. A 931, 1114 (2014)

[45] L.Adamczuk et al. (STAR Collaboration) Phys.Rev.C 96 (2017) 4, 044904

[46] A.Z.Mekjian, Phys. Rev. Lett. 38, 640 (1977); Phys. Rev. C 17, 1051 (1978); and Nucl. Phys. A 312, 491 (1978).

[47] J.I.Kapusta, Phys. Rev. C 21, 1301 (1980).

[48] PDG group review, J. Phys. G 37, 075021 (2010), Introduction, section 5.2

[49] I.G.Bearden et al. (NA44 Collaboration), Eur. Phys. J. C 23, 237–247 (2002).

[50] T.A.Armstrong et al. (E864 Collaboration), Phys. Rev. C 61, 064908 (2000), nucl-ex/0003009

[51] J.Barrette et al. (E877 Collaboration), Phys. Rev. C61,044906 (2000]

[52] M.J.Bennett et al. (E878 Collaboration), Phys. Rev. C58, 1155 (1998).

[53] G.Ambrosini et al. (NA52 Collaboration), Phys. Lett. B 417, 202 (1998)

[54] M.Abdulhamid et al., STAR Collaboration, Phys.Rev.Lett. 130 (2023) 202301

[55] D.Zhang (STAR Collaboration), Nucl. Phys. A 1005, 121825 (2021).

[56] arXiv:2311.11020 [nucl-ex]

[57] I.G. Bearden et al. (BRAHM Collaboration), Phys. Rev. Lett. 93, 102301, 2004.

[58] F.Videbaek and Ole Hansen, Phys. Rev. C 52 (1995) 2684.

[59] S.A.Bass et al., Prog. Part. Nucl. Phys. 41 225 (1998).

[60] B.Hong et al (FOPI Collaboration), Phys. Rev. C 57 (1998) 244.

[61] J. Bachler et al (NA35 Collaboration), Phys. rev. Lett. 72 (1994) 1419.

[62] B.B.Back et al (E917 Collaboration), Phys. Rev. Lett. 86 (2001) 1970.

[63] C. Blume, for the NA49 Collaboration, J. Phys. G 34 (2007) S951.

[64] M. J. Murray, J. Phys. G 28, 2069 (2002).

[65] B. Tomasik and U. Heinz, Phys. Rev. C 65, 031902(R) (2002).

[66] L. P. Csernai and J. I. Kapusta, Phys. Rep. 131, 4 (1986) 223—318.

[67] S. Z. Belenkij and L. D. Landau, Nuovo Cimento, Supplement 3, 15 (1956).

[68] G. Poggi et al (FOPI Collaboration), Nucl. Phys. A 586, 755 (1995).

[69] L. Ahle et al (E802 Collaboration) Phys. Rev. C 60, 064901 (1999).

[70] T. Anticic et al (NA49 Collaboration), Phys. Rev. C 69, 024902 (2004).

[71] C. Alt et al (NA49 Collaboration), Phys. Rev. C 77, 024903 (2008).

[72] T.Anticic et al. (NA49 Collaboration) Phys.Rev.C 85 (2012) 044913

[73] T.A. Armstrong et al (E864 Collaboration) Phys. Rev. C 61,064908 (2000).

[74] J. Cleymans, H. Oeschler, K. Redlich, and S. Wheaton, Phys. Rev. C 73, 034905 (2006).

[75] The STAR Collaboration, Phys. Rev. C 96,044904 (2017).

[76] K.-J.Sun et al., Phys.Lett.B 774 (2017) 103

[77] D.Oliinychenko, Nucl.Phys.A 1005 (2021) 121754

[78] M.Abdulhamid et al. (STAR Collaboration), Phys.Rev.Lett. 130 (2023) 202301.